ISSN 1349-1113
JAXA-RR-04-035E

JAXA Research and Development Report

Comparative Force/Heat Flux Measurements between JAXA Hypersonic Test Facilities Using Standard Model HB-2 (Part 1: 1.27 m Hypersonic Wind Tunnel Results)

Shigeru KUCHI-ISHI, Shigeya WATANABE, Shinji NAGAI,
Shoichi TSUDA, Tadao KOYAMA, Noriaki HIRABAYASHI,
Hideo SEKINE, and Koichi HOZUMI

March 2005

Japan Aerospace Exploration Agency

Comparative Force/Heat Flux Measurements between JAXA Hypersonic Test Facilities Using Standard Model HB-2 (Part 1: 1.27 m Hypersonic Wind Tunnel Results)

Shigeru KUCHI-ISHI[*1], Shigeya WATANABE[*1], Shinji NAGAI[*1],
Shoichi TSUDA[*1], Tadao KOYAMA[*1], Noriaki HIRABAYASHI[*1],
Hideo SEKINE[*2], and Koichi HOZUMI[*2]

HB-2形状標準模型を用いたJAXA極超音速風洞間力／加熱率対応風試（その１：1.27 m極超音速風洞測定結果）

口石　茂[*1]、渡辺重哉[*1]、永井伸治[*1]、津田尚一[*1]
小山忠勇[*1]、平林則明[*1]、関根英夫[*2]、穂積弘一[*2]

ABSTRACT

This report presents a detailed description and results of force and heat flux measurement tests conducted in the 1.27 m Hypersonic Wind Tunnel (HWT) of the Japan Aerospace Exploration Agency (JAXA). The HB-2 standard hypersonic ballistic configuration was employed as a model. The force-measuring tests used a stainless steel model on a six-component balance, and the heat flux measurement tests were made using a chromel model with a total of 28 coaxial thermocouples press-fitted on the surface. A non-intrusive heat flux measurement was also made by infrared (IR) thermography using an alternative nose part made of polyimide plastic. The tests were conducted at a nominal Mach number of 10, a stagnation enthalpy of 1 MJ/kg, and stagnation pressures from 1 to 6 MPa. For both force and heat tests, good data repeatability was confirmed. The heat transfer coefficient obtained from the IR thermography agreed well with that from the thermocouple measurement. For the heat flux data, uncertainties associated with flow repeatability, the model's streamwise location in the test section, and the model's alignment were quantified and examined. Also, the measurement error of both the force and heat tests was evaluated. A conventional statistical approach which estimates the bias and random error components was applied to the force test data, while a Monte Carlo approach was used to numerically estimate the uncertainty in the data reduction process for the heat flux data. The present experiment was conducted as a series of comparison tests between two hypersonic facilities in JAXA. Since the free-stream conditions and the corresponding experimental data were tabulated in detail for each run, the present test data serve as a database not only for the evaluation of force and heat flux measurement in HWT, but also for the validation of hypersonic computational fluid dynamics (CFD) codes.

Keywords: hypersonic wind tunnel, standard model, aerodynamic force, heat flux, uncertainty analysis

概　　要

本報告は、JAXA 1.27 m極超音速風洞（HWT）において実施された、HB-2形状バリスティック標準模型を用いた空気力/空力加熱率測定試験結果に関するものである。加熱率測定試験で用いられた模型はクロメル製であり、計28個の同軸熱電対が装着されている。模型頭部はベスペル製部品と交換し、赤外線カメラによる非接触計測の結果と比較が可能となっている。試験は風洞澱み温度1000 K、澱み圧力１－6 MPaの範囲で実

＊1　Wind Tunnel Technology Center, Institute of Space Technology and Aeronautics（総合技術研究本部風洞技術開発センター）
＊2　Foundation for Promotion of Japanese Aerospace Technology（航空宇宙技術振興財団）

施された。力試験/熱試験ともに、気流再現性、模型射出位置、モデル取りつけ精度に関するデータのばらつきを定量的に評価した。データ再現性は良好で、HWTの良好な気流特性を示す結果となった。力試験については、過去実施された他風洞における試験データと比較し、良好な一致が確認された。また力試験、熱試験共に不確かさ解析を実施した。力試験については従来用いられる統計的手法を適用し、得られた誤差幅は測定で得られたデータのばらつきと比較して妥当であることが確認された。一方熱試験についてはモンテカルロ法による不確かさの数値的導出を試み、低加熱率においては温度測定値のばらつきが、高加熱率の場合は熱物性値の不確かさが総合的な不確かさに対して支配的であることがわかった。本試験は、航技研極超音速関連風洞対応風試の一環として実施されたものである。また本試験データは極超音速流におけるCFDコード検証においても有用である。

NOMENCLATURE

A = Reference area, $\pi D^2/4$
A_b = Model base area
B = Bias limit
C_A = Zero-lift gross (total) axial force coefficient, $F_x/q_\infty A$
C_{AF} = Zero-lift forebody axial force coefficient, $C_A - (p_\infty - p_b) A_b/A$
C_m^B = Pitching-moment coefficient based on the balance center, $M_y/q_\infty AD$
C_m = Pitching-moment coefficient based on the reference point, $C_m^B - dC_N/D$
C_N = Normal force coefficient, $F_z/q_\infty A$
c = Specific heat
D = Reference centerbody diameter (see Fig. 2)
d = distance from the balance center to the moment reference point
F_x = Axial aerodynamic force measured by the balance
F_z = Normal aerodynamic force measured by the balance
h = Heat transfer coefficient, $q/(T_{aw} - T_w)$
k = Thermal conductivity
L = Distance from the nozzle exit (see Table C2)
M_y = Pitching moment measured by the balance
M = Mach number
P = Precision limit, tS
P_{pit} = Pitot pressure
P_0 = Tunnel stagnation pressure
p = Pressure
p_b = Base pressure
q = Heat flux, dynamic pressure
R = Gas constant
Re = Free-stream Reynolds number based on centerbody diameter
S = Precision index
T = Temperature
T_{aw} = Adiabatic temperature
T_0 = Tunnel stagnation temperature, initial temperature
t = Time, Student t value
t_0 = Initial time
U = Velocity, total uncertainty, random variable
x = Axial distance
α = Angle of attack
ϕ = Roll angle
θ = Circumferential position
ρ = Density
γ = Specific heat ratio

Subscripts
w = Model surface (wall)
0 = Stagnation
∞ = Free-stream

1. INTRODUCTION

For the design and development of future hypersonic flight vehicles, the prediction of aerothermal characteristics during the atmospheric reentry is of importance. Due to limitations of conventional ground-based experimental facilities, it is practically impossible to produce flows of desired Mach number, Reynolds number, and total enthalpy exactly the same as those in actual flight conditions. As well, a numerical prediction applying computational fluid dynamics (CFD) techniques to date is insufficient in terms of reliability since it includes many uncertainties for both numerical and physical aspects. Therefore, it is apparent that the use of either experimental or numerical approach alone is inadequate for a reliable flight prediction and it is the best way to apply all of possible approaches and to evaluate the prediction accuracy from a global point of view.

The Japan Aerospace Exploration Agency (JAXA) has two large-scale hypersonic facilities called the 1.27 m Hypersonic Wind Tunnel (HWT) and the High Enthalpy Shock Tunnel (HIEST). These facilities are common in the sense that they cover hypersonic speeds, but there are differences regarding the flow properties and tunnel specifications. Specifically, HWT is a blowdown type wind tunnel and therefore its flow properties can be estimated relatively accurately. But the stagnation enthalpy attainable in HWT is approximately 1 MJ/kg and is much lower than actual flight conditions at hypersonic speeds. On the contrary, in HIEST, although much higher enthalpy levels up to 25 MJ/kg can be obtained, there are many unknown factors inherent to the high-enthalpy short duration facilities. Hence it is meaningful to use these facilities in a synergistic way, such that the strength of one facility compensates for a weakness of the other. In other words, one facility should be used to improve capability and/or accuracy of the other such that both facilities benefit.

From this viewpoint, in JAXA, a comparative test program was performed for the above two facilities to obtain force/heat flux data using the same model configuration. Through the synergistic use of these facilities together with the aid of CFD prediction technique, we expect to have a practical guideline for accurate and reliable prediction of aerothermodynamic properties of actual flight vehicles.

In the present report, results are presented for the force/heat flux measurement test conducted in the HWT using a ballistic-type model configuration. The tests were conducted at conditions of the stagnation enthalpy around 1 MJ/kg and the stagnation pressures from 1 to 6 MPa. For the force test, the three-component aerodynamic force data are compared with existing experimental results obtained at other hypersonic facilities. To obtain heat flux data, two measurement techniques were applied and the results are compared to assess quantitative reliability of the data. An uncertainty analysis was also performed to evaluate the measurement uncertainty both for the force and heat test. In the force test, a systematic approach to estimate both bias and random errors for each experimental stage based on the statistical viewpoint was used. In turn, since the data reduction includes a numerical integration procedure for the heat test, a sophisticated method to apply Monte Carlo technique was adopted to estimate overall uncertainty of the heat flux reduction process. The predicted uncertainties are then compared with random errors estimated from repeat tunnel runs of the present force/heat test.

In this report, the experimental data and corresponding free-stream conditions are tabulated in detail as appendix and therefore this report is expected to be useful for the purpose of validating hypersonic CFD codes.

2. FACILITY

A schematic view of HWT is shown in Fig. 1. HWT is a blowdown cold type wind tunnel with nominal Mach number of 10. To prevent liquefaction of air, a pebble bed heater heated by a line gas burner is utilized. The humidity management system including the combustion gas replacement system keeps the humidity in the working gas below 50 ppmV at a reservoir pressure of 4 MPa. A previously conducted flow calibration test showed that the Mach number uncertainty is less than 0.3% in the core flow part.

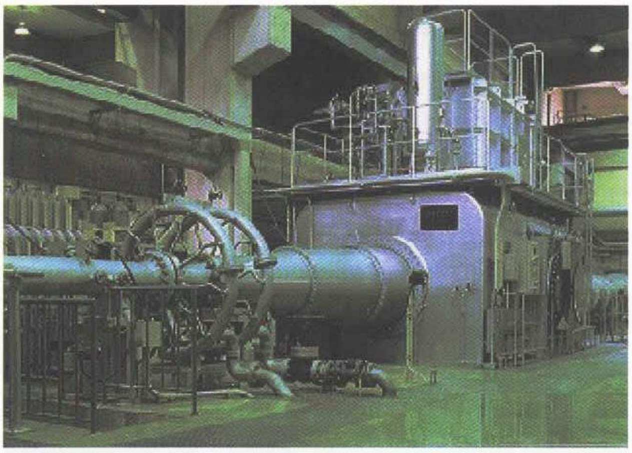

Fig. 1 JAXA 1.27 m Hypersonic Wind Tunnel (HWT).

The basic test procedure of HWT is as follows. After the start of blowdown, a model is injected into or withdrawn out of the flow by a model support system in the force measurement and by a rapid injection system in the heat flux measurement, respectively. The main model support system is capable of changing the model pitch angle continuously (sweep operation) or step-wise (pitch-and-pause operation) during a tunnel run. The rapid injection system enables the model to be situated in the center of the flow within 0.2 seconds from out of the flow so that the assumption of step heating, required to reduce the heat flux from the IR camera data using the one-dimensional heat conduction theory, becomes appropriate. A detailed description of HWT facility is found in Ref. [1].

3. MODELS

3.1 Model configuration

In the present study, a relatively simple model configuration was employed because it is preferable to minimize uncertainties coming from the geometry complexity from the viewpoint of tunnel-to-tunnel comparison. The HB-2 type model employed in the

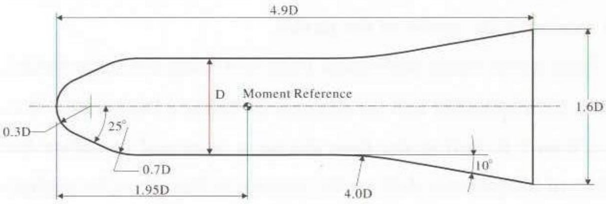

Fig. 2 HB-2 configurations.

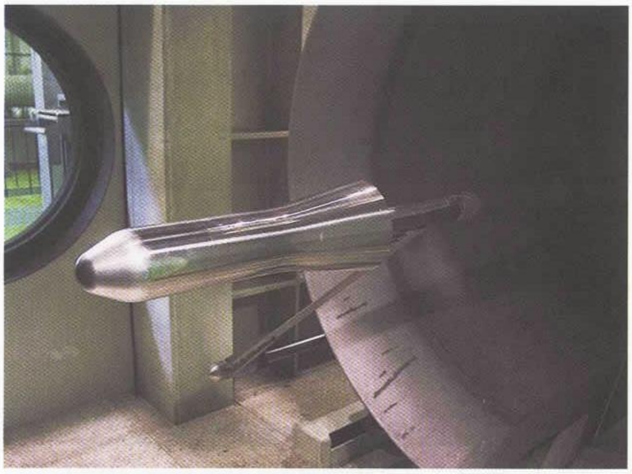

(a)

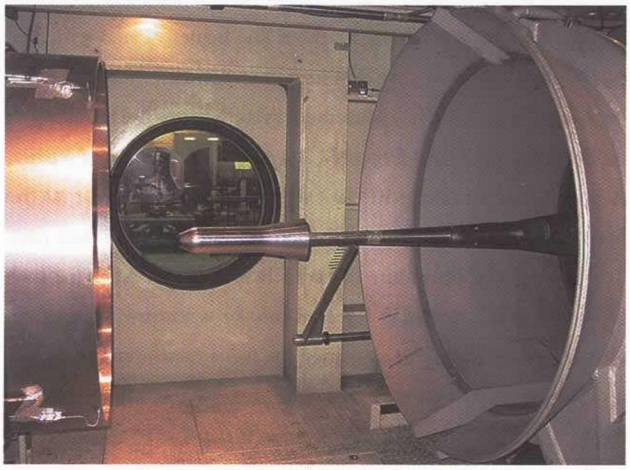

(b)

Fig. 3 HB-2 force model.
(a) Model close-up view
(b) With model support system

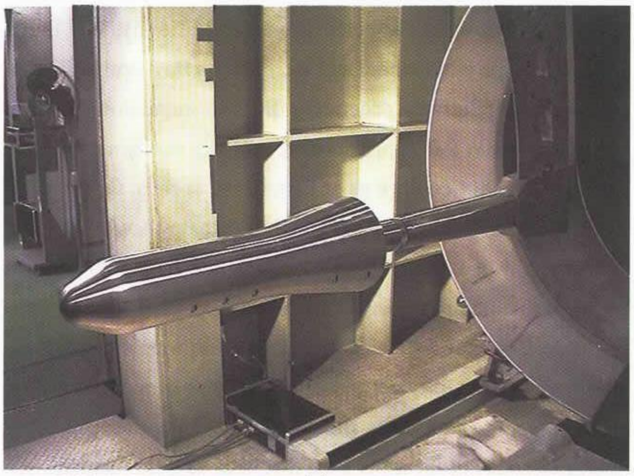

(a)

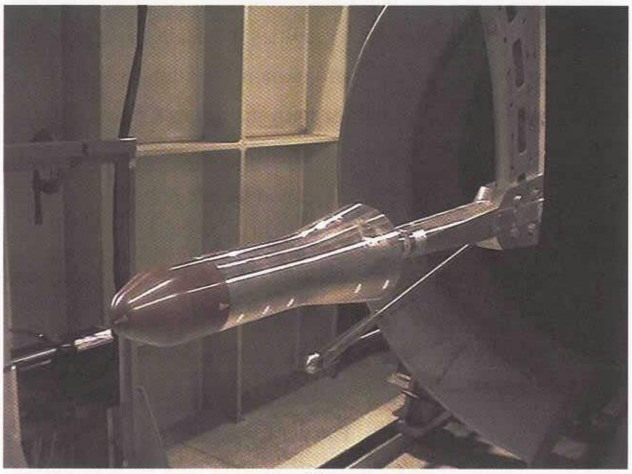

(b)

Fig. 4 HB-2 heat model.
(a) Chromel nose parts
(b) Polyimide nose parts

present test is a standard model proposed in a joint program of AGARD and Supersonic Tunnel Association (STA) in 1950–60's [2]. This has an analytical shape that consists of a sphere, cone, cylinder, and flare as shown in Fig. 2.

3.2 Force model

The force model used in the present study is shown in Fig. 3 a) and b). The model is made of a stainless steel (SUS304) and the weight is 12.675 kg without the balance. The length and the centerbody diameter of the model are 490 mm and 100 mm, respectively. A six-component balance (Nissho LMC-6522-33/Z100) was installed inside the model, and the balance center was set to be located at the center of the model.

From a previously performed force test using the same model, it has been appeared that the increase of balance temperature was less than 1 K during the flow duration time and therefore the effect of temperature drift on the balance is thought to be negligible. On the other hand, in order to perform base pressure correction, a total of three pressure sensors (Kulite Semiconductor XCS-093-5A) were installed on the model base plate (two points) and inside the model (one point). A detailed schematic of the model is illustrated in Fig. A1 of Appendix A.

3.3 Heat model

The heat model are shown in Fig. 4 a) and b). The dimension is the same as that of the force model. In this model, a total of 28 chromel-constantan type co-axial thermocouples of 1.5 mm diameter (Medtherm TCS-E-10370) were press-fitted. The position of each sensor is illustrated in Fig. A2 and Table A1 of Appendix A.

A total of 8 sensors are circumferentially located in the flare part to quantify uncertainties coming from the model alignment/flow deflection error at zero angle of attack. The model is made of chromel in order to avoid electromotive force caused by the difference of thermoelectric properties between the material of the model surface and the outer tube of the thermocouple [3].

The nose parts (29% of the total length, see Fig. 4) can also be changed with Dupont Vespel® polyimide plastic part which is used for the non-intrusive surface temperature measurement using infrared (IR) thermography technique. Vespel was selected as a material since it is suitable from the viewpoint of homogeneity, low thermal conductivity, machinability, and decay durability against the high temperature environment.

4. EXPERIMENTAL PROCEDURE

4.1 Test conditions

In Table 1, four standard operating conditions of HWT are tabulated. The stagnation enthalpy is nearly constant irrespective of the change in the stagnation pressure and is approximately 1 MJ/kg. The unit Reynolds number ranges from 0.9×10^6 to 4.3×10^6/m.

As already mentioned, for the force test, two model injection methods of the sweep and pith-and-pause operation can be selected. The angle of attack ranges from −10 to 32 degrees for both operations. For the sweep operation mode, the sweep angle was divided into two parts ($\alpha = -10 \sim 18$ and $16 \sim 32$ degrees) due to the limitation of flow duration time. For the pitch-and-pause operation, data were obtained at five angles of attack ($\alpha = -10$, 0, 10, 20, and 30 degrees) and the pause period was set to 2.5 ~ 3.0 seconds at each angle of attack. A total of five repeat runs were performed in the case of $P_0 = 1$ MPa to estimate random error from a statistical uncertainty analysis.

For the heat test, two angles of attack (0 and 15 degrees) were selected. Similar to the force test, five repeat runs were performed in the case of $P_0 = 2.5$ MPa to estimate the random error. As well, the model stream-wise location in the test section was changed to evaluate uncertainties coming from stream-wise flow non-uniformity. This was done by shifting the model injection position from the standard position (500 mm from the nozzle exit) to 230 mm upstream or to 450 mm downstream. For the nose part of the model, a non-intrusive measurement using the infrared thermography was also conducted.

Photographs of the rapid injection system and the infrared camera placed in the test section are provided in Figs. 5 and 6, respectively.

Table 1 HWT standard tunnel and free-stream conditions.

P_0 (MPa)	1	2.5	4	6
T_0 (K)	870-970	920-1020	950-1030	1000-1070
M_∞	9.46	9.59	9.65	9.69
p_∞ (Pa)	33	75	115	168
T_∞ (K)	51	52	53	55
ρ_∞ (g/m^3)	2.3	5.0	7.6	10.6
Re ($\times 10^6$ 1/m)	0.9	2.1	3.1	4.3

The list of run schedules and corresponding free-stream conditions are summarized in Table C1 of the Appendix C for the force test and C2 for the heat test, respectively. Care was taken not to perform consequent runs on the same day. For example, each repeat run was made one or two days apart to avoid comparing two consecutive runs on the same day. This aids in estimating the overall measurement system repeatability [4].

4.2 Data acquisition/reduction

As for the force test, the three-component balance outputs corresponding total axial force, normal force, and pitching moment were converted to the aerodynamic coefficient by dividing the dynamic pressure and reference area (plus reference length for the pitching moment coefficient).

The loads acting on the balance are a combination of the aerodynamnic loads and the weight of the model. To extract the aerodynamic loads, the balance output must be corrected to remove the effects of the model weight, which is termed as static weight

Fig. 5 Rapid injection system.

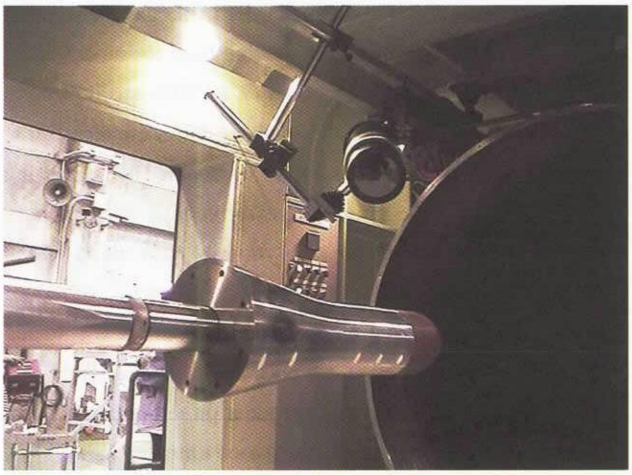

Fig. 6 Infrared camera system.

tare. The static tare data were obtained at the beginning of the test campaign without blowing (wind-off), and were subtracted from the wind-on data to correct the variation of the model weight load with considering the sting/balance bending effects throughout the run.

In a hypersonic wind tunnel testing, the static pressure is too low to measure accurately and it is not practical to determine the free-stream Mach number from the nozzle wall pressure. Therefore the Mach number is computed from the stagnation pressure and temperature measured at the reservoir together with the pitot pressure measured in the test section. Since the pitot pressure sensor cannot be placed simultaneously with a model, in HWT, a calibration test using a number of pitot pressure sensors was conducted and the Mach number was computed in advance. The dynamic pressure was then calculated from the calibrated Mach number and the stagnation pressure and temperature measured at each run of the present force and heat tests. A detailed description concerning the method of computing free-stream properties is found in Appendix B.

The total axial force coefficient C_A is converted to the forebody axial force coefficient C_{AF} through the base pressure correction as

$$C_{AF} = C_A - \frac{(p_\infty - p_b) A_b}{q_\infty A} \tag{1}$$

where A and A_b are the reference area and the area of the model base, respectively. On the other hand, the pitching moment coefficient is first evaluated around the balance center, and is transferred to the value around the moment reference point as

$$C_m = C_m^B - \frac{d}{D} C_N \tag{2}$$

where d is the distance from the balance center to the moment reference point (see Figs. 2 and A1).

For the heat flux measurement test, time history of the sensor voltage was recorded in a data recorder (Yokogawa analysing recorder AR 4800) for 5 seconds starting from the model injection time. A cold junction unit (Chino KT-C020) was utilized to set the reference temperature. The voltage data were recorded at a sampling frequency of 1 kHz and were smoothed by the moving average technique. The smoothed sensor voltage was then converted to temperature using a polynomial expression which relates the thermoelectric voltage to the temperature. To reduce aerodynamic heating from the thermocouple data, it is assumed that 1) heat conduction along the body surface is negligible, and 2) thermal properties are not dependent on temperature. With denoting the temperature measured at each time step $(t_0, t_1, \cdots t_n)$ as $(T(t_0), T(t_1), \cdots T(t_n))$, the model surface heat flux at time t_n is evaluated by applying the formula of Cook and Felderman [5], [6], which is written as

$$q(t_n) = 2\sqrt{\frac{\rho c k}{\pi}} \sum_{i=1}^{n} \frac{T'(t_i) - T'(t_{i-1})}{\sqrt{t_n - t_i} + \sqrt{t_n - t_{i-1}}} \tag{3}$$

where T' denotes temperature increment from the initial value, i.e., $T'(t_i) = T(t_i) - T(t_0)$. As for the thermal properties, a constant chromel value at 300 K ($\rho c k = 6.395 \times 10^7$ J^2/m^{4}K^{2}s) was taken from Ref. [7]. Finally, the computed time history of the heat flux was averaged in time to reduce a time-averaged value for each tunnel run.

For the IR thermography tests, the IR camera measurement system was used. The IR camera measurement system consists of an infrared camera (AGEMA 900LW) and a computer equipped with a digitizer. The infrared image obtained was allocated to the body surface through the three-dimensional image mapping. In reducing aerodynamic heating from the image mapping data, the method of Jones and Hunt was applied [8]. In this method, by assuming a constant heat transfer coefficient h and step heating, the analytical solution of the one-dimensional heat conduction equation at time t (after the start of step heating) is available as

$$\frac{\mathrm{T}(t) - \mathrm{T}(t_0)}{T_{aw} - T(t_0)} = 1 - \exp(\beta^2)\mathrm{erf}(\beta) \tag{4}$$

where

$$\beta = h\sqrt{\frac{t}{\rho c k}} \tag{5}$$

The parameter β can be computed numerically from Eq. (4) by specifying the initial temperature $T(t_0)$, measured temperature at time t, $T(t)$, and the adiabatic temperature T_{aw} (assumed to be equal to the tunnel stagnation temperature T_0). The heat transfer coefficient can then be obtained from Eq. (5). In this method, only an initial temperature and a temperature at a time during a tunnel run are required; i.e., no temperature time history is needed. This is important for an imaging method since a large amount of data space is required to store image files of the temperature time history [9].

Also in this method, it is assumed that the thermal properties ρ, c, and k are constant with respect to temperature. To correct the temperature dependence, an effective temperature T_{JH} was introduced which is given as

$$T_{JH} = T(t_0) + [T(t) - T(t_0)] \times F \tag{6}$$

The thermal properties were then evaluated at this reference temperature using a Vespel thermal properties curve fit. The factor F

was empirically set to 0.6 and it has been shown that the effect of thermal properties variation can be corrected within 1% accuracy by using this value.

In a strict sense, as the model passes through the test section wall boundary layer, the assumption of step heating does not hold true. Therefore the model injection process was modeled as step heating by correcting the time t in Eqs. (4) and (5) so that the heat transfer coefficient linearly increases from zero to h and become constant in the middle part of the wall boundary layer.

5. UNCERTAINTY ANALYSIS

5.1 Force test uncertainty

One conventional approach to estimate the accuracy of measurement data is to assume the error (defined as the difference between the experimentally determined value and truth) to be composed of two components, namely bias and random errors. The random error is defined as an uncertainty coming from the scattering of the data, while the bias error is a systematic error which is invariant throughout the test. Practically, both components are to be quantified at each experimental process (i.e., calibration, data acquisition, and data reduction). These components are then summed up to evaluate the overall uncertainty at a specific level of confidence. The 95% confidence uncertainties for the present force test were estimated using the methodology described in Refs. [10] and [11].

To estimate the bias and random errors, a bias limit B and a precision limit P are defined. Each limit is estimated by an interval within which the true value of a variable lies. Specifically, the precision limit is given as

$$P = tS \tag{7}$$

where t is called the Student t value and can be determined from the degree of freedom which is a measure of data independency. The value S is the standard deviation of a sample of N readings for a variable x, and S^2 is called the *unbiased estimate of population variance* which is defined as

$$S^2 = \sum_{k=1}^{N} (x_k - \bar{x})^2/(N-1) \tag{8}$$

and the mean value $\bar{x}$ is defined as

$$\bar{x} = \sum_{k=1}^{N} x_k/N \tag{9}$$

Finally the 95% confidence uncertainty U is given by the root-sum-square of the bias and precision limit as

$$U = \sqrt{B^2 + P^2} \tag{10}$$

In the present case, we need to estimate the uncertainty concerning the aerodynamic coefficients C_{AF} , C_N, and C_m. Of the three, the expression of the forebody axial force coefficient C_{AF} found in Eq. (1) is rewritten as

$$C_{AF} = \frac{F_x - (p_\infty - p_b)A_b}{q_\infty \mathrm{A}} \tag{11}$$

Hence the possible error includes uncertainties concerning the axial aerodynamic force F_x, free-stream pressure p_∞, base pressure p_b, and free-stream dynamic pressure q_∞.

In the HWT experiment, the dynamic pressure is computed from the following relation

$$q_\infty = \frac{\gamma}{2} p_\infty M_\infty^2 \tag{12}$$

where $\gamma = 1.4$ is the specific heat ratio. Note that the free-stream Mach number is not dependent on each run but is a specified value which was determined by the calibration test conducted in advance. The free-stream static pressure p_∞ is also reduced from the calibrated Mach number with the tunnel stagnation pressure/temperature measured at each tunnel run. Thus the uncertainty in q_∞ should be estimated as a combination of each elemental error for M_∞, P_0, and T_0.

As a first step, the uncertainty in the free-stream Mach number M_∞ is estimated. As described in Appendix B, the local Mach number M_i obtained at each point in the test section is a function of the tunnel stagnation pressure P_0, stagnation temperature T_0, and pitot pressure P_{pit}. Table 2 summarizes the measurement uncertainties of the tunnel properties.

Both bias and precision limits of the tunnel stagnation pressure were reduced from calibration data of the pressure sensor, while both error components were empirically determined for the stagnation temperature. The pitot pressure was measured at each local point in the test section using electronically scanned pressure (ESP) modules and hence its uncertainties were estimated from calibration data of the ESP module.

Using these three measured properties, the Mach number at each local point is computed based on the one-dimensional isentropic relations with a caloric gas imperfections correction method found in Ref. [12]. The concrete procedure of the Mach number reduction method is described in Appendix B. Thus the bias and precision limits concerning the Mach number uncertainty can be estimated as a combination of each error component

$$B_{M_i} = \left[\left(\frac{\partial M_i}{\partial P_0} B_{P_0}\right)^2 + \left(\frac{\partial M_i}{\partial T_0} B_{T_0}\right)^2 + \left(\frac{\partial M_i}{\partial P_{\mathrm{pit}}} B_{P_{\mathrm{pit}}}\right)^2\right]^{1/2} \tag{13}$$

Table 2 Estimated uncertainties in the HWT tunnel and free-stream properties.

Stagnation pressure (Pa)	Typical value	1000000	2500000	4000000	6000000
	B	207	207	207	587
	S	1533	1533	1533	6212
	U	3422	3422	3422	14066
Stagnation temperature (K)	Typical value	920	970	990	1030
	B	30	30	30	30
	S	5	5	5	5
	U	31.7	31.7	31.7	31.7
Pitot pressure (Pa)	Typical value	3578	8945	14312	21468
	B	3.1	3.1	3.1	3.1
	S	5.5	5.5	5.5	5.5
	U	11.6	11.6	11.6	11.6
Mach number	Typical value	9.46	9.59	9.65	9.69
	B	0.011	0.010	0.010	0.010
	S	0.014	0.014	0.013	0.011
	U	0.029	0.030	0.028	0.025
Dynamic pressure (Pa)	Typical value	2135	5010	7788	11459
	B	16	37	55	79
	S	15	35	50	65
	U	34	78	113	149

$$P_{M_i} = \left[\left(\frac{\partial M_i}{\partial P_0} P_{P_0}\right)^2 + \left(\frac{\partial M_i}{\partial T_0} P_{T_0}\right)^2 + \left(\frac{\partial M_i}{\partial P_{\mathrm{pit}}} P_{P_{\mathrm{pit}}}\right)^2\right]^{1/2} \tag{14}$$

The partial derivatives found in the above equations are called *sensitivity coefficients* which represent the contribution of each error component on the overall uncertainty. Since the Mach number reduction process includes a nonlinear operation, it is impossible to analytically obtain these derivatives. Thus, in the present case, they were evaluated by a numerical differentiation technique.

The free-stream Mach number M_∞ is given as an average of the local values as

$$M_\infty = \sum_{i=1}^{N} M_i / N \tag{15}$$

where N is the number of measurement point in the test section. Hence the free-stream Mach number uncertainty includes a component concerning the scattering of each sensor data in addition to the bias/random contributions of the ESP module. The resulting Mach number uncertainties are shown in Table 2.

Now the bias and precision limits for the dynamic pressure are estimated as

$$B_{q_\infty} = \left[\left(\frac{\partial q_\infty}{\partial P_0} B_{P_0}\right)^2 + \left(\frac{\partial q_\infty}{\partial T_0} B_{T_0}\right)^2 + \left(\frac{\partial q_\infty}{\partial M_0} B_{M_{\mathrm{pit}}}\right)^2\right]^{1/2} \tag{16}$$

$$P_{q_\infty} = \left[\left(\frac{\partial q_\infty}{\partial P_0} P_{P_0}\right)^2 + \left(\frac{\partial q_\infty}{\partial T_0} P_{T_0}\right)^2 + \left(\frac{\partial q_\infty}{\partial M_0} P_{M_{\mathrm{pit}}}\right)^2\right]^{1/2} \tag{17}$$

In this case, the sensitivity coefficients are evaluated analytically by differentiating Eq. (12) with respect to P_0, T_0, and M_∞. However, since p_∞ in Eq. (12) is also a function of P_0, T_0, and M_∞, the process is somewhat complex and hence they were also evaluated numerically in the present analysis. The estimated dynamic pressure uncertainties are tabulated in Table 2.

In the next step, the uncertainty in the aerodynamic force measurements are considered. The uncertainty in the balance output consists of error components concerning the balance calibration and the strain amplifier adjustment using a calibration strain generator. The level of these error sources were evaluated for both bias and precision limits from cataloged data. The total uncertainty was found to be around 0.1% of the balance capacity for each force component. As mentioned in the preceding section, in the reduction of aerodynamic forces, the static tare data obtained before the experiment are subtracted from the balance output for each angle of attack. Thus the aerodynamic force at each angle of attack includes uncertainties concerning the static tare measurement, wind-on force measurement, and angle of attack interpolation. Both for wind-on and static tare measurements, the bias limit is equal to that of the balance output, while the scattering of the data during the measurement was added to evaluate the precision limits. The aerodynamic force uncertainties coming from the angle of attack interpolation were reduced from the estimated angle of attack error. The resulting bias and precision limits of these error sources are combined to calculate the total uncertainty in the aerodynamic force measurements in Table 3.

Finally the aerodynamic forces F_x and F_z are converted to the aerodynamic coefficients C_{AF} and C_N by dividing the dynamic pressure and the reference area. In the present case, the base pressure contribution to the overall uncertainty in C_{AF} was found to be negligible and omitted. In this case, the overall uncertainty in C_{AF} can be estimated as

$$B_{C_{AF}} = \left[\left(\frac{\partial C_{AF}}{\partial F_x} B_{F_x}\right)^2 + \left(\frac{\partial C_{AF}}{\partial q_\infty} B_{q_\infty}\right)^2\right]^{1/2} \tag{18}$$

Table 3 Estimated uncertainties in the aerodynamic force measurement.

	Component	F_x (N)	F_y (N)	F_z (N)	M_x (Nm)	M_y (Nm)	M_z (Nm)
	Full scale	245	490	981	15	74	49
Static tare measurement	B	0.043	0.097	0.20	0.007	0.024	0.015
	S	0.25	0.40	0.35	0.013	0.028	0.020
	U	0.49	0.79	0.71	0.026	0.060	0.041
Wind-on measurement	B	0.043	0.097	0.20	0.007	0.024	0.015
	S	0.24	0.40	0.34	0.013	0.029	0.020
	U	0.48	0.80	0.69	0.026	0.061	0.041
Angle of attack	B	0.048	0.021	0.013	0.000	0.000	0.000
	S	0.047	0.020	0.013	0.000	0.000	0.000
	U	0.11	0.046	0.029	0.000	0.000	0.001
Total	B	0.08	0.14	0.29	0.010	0.033	0.021
	S	0.35	0.56	0.48	0.018	0.040	0.028
	U	0.69	1.12	0.99	0.037	0.086	0.058

$$P_{C_{AF}} = \left[\left(\frac{\partial C_{AF}}{\partial F_x} P_{F_x}\right)^2 + \left(\frac{\partial C_{AF}}{\partial q_\infty} B_{q_\infty}\right)^2\right]^{1/2} \tag{19}$$

$$U_{C_{AF}} = [(B_{C_{AF}})^2 + (P_{C_{AF}})^2]^{1/2} \tag{20}$$

This is possible since there is no correlation between F_x and q_∞. If the base pressure correction term is included, the partial derivative of C_{AF} should be evaluated with respect to the independent variables P_0, T_0, and M_∞ instead of q_∞. The partial derivatives $\partial C_{AF}/\partial q_\infty$ and $\partial C_{AF}/\partial F_x$ can be evaluated readily by directly differentiating Eq. (11) with respect to F_x and q_∞. The uncertainty in the normal force coefficient C_N can be reduced by the same procedure.

On the other hand, the pitching moment coefficient around the moment reference point C_m is computed from the pitching moment around the balance center C_m^B as

$$C_m = C_m^B - \frac{d}{D} C_N \tag{21}$$

Hence the bias and precision limits for the pitching moment coefficient are evaluated as

$$B_{C_m} = \left[\left(\frac{\partial C_m}{\partial C_m^B} B_{C_m^B}\right)^2 + \left(\frac{\partial C_m}{\partial d} B_d\right)^2 + \left(\frac{\partial C_m}{\partial C_N} B_{C_N}\right)^2 + 2\frac{\partial C_m}{\partial C_m^B}\frac{\partial C_m}{\partial C_N} B_{C_m^B} B_{C_N}\right]^{1/2} \tag{22}$$

$$P_{C_m} = \left[\left(\frac{\partial C_m}{\partial C_m^B} P_{C_m^B}\right)^2 + \left(\frac{\partial C_m}{\partial d} P_d\right)^2 + \left(\frac{\partial C_m}{\partial C_N} P_{C_N}\right)^2\right]^{1/2} \tag{23}$$

$$U_{C_m} = [B_{C_m}^2 + P_{C_m}^2]^{1/2} \tag{24}$$

The bias limit includes a cross term which correlates C_m^B and C_N since the uncertainties of the pitching moment and the normal force arise from the same source and are presumed to be perfectly correlated.

Table 4 Estimated uncertainties in the aerodynamic coefficients at angle of attack of 15 degrees

	P_0 (MPa)	1	2.5	4	6
C_{AF}	Typical value	0.767	0.723	0.722	0.712
	B	0.007	0.004	0.004	0.005
	S	0.021	0.009	0.006	0.006
	U	0.043	0.018	0.013	0.012
C_N	Typical value	1.175	1.140	1.174	1.169
	B	0.019	0.009	0.008	0.009
	S	0.030	0.013	0.009	0.008
	U	0.062	0.027	0.019	0.019
C_m	Typical value	-1.092	-1.050	-1.098	-1.090
	B	0.030	0.013	0.010	0.009
	S	0.028	0.013	0.009	0.007
	U	0.063	0.028	0.020	0.016

The resulting predicted uncertainties for each aerodynamic force coefficient are tabulated for the case of $\alpha = 15$ degrees in Table 4.

5.2 Heat test uncertainty

As described previously, the heat flux is evaluated from the temperature time history of the thermocouples by using Eq. (3), which is rewritten as

$$q(t_n) = 2\sqrt{\frac{\rho c k}{\pi}} \sum_{i=1}^{n} \frac{T'(t_i) - T'(t_{i-1})}{\sqrt{t_n - t_i} + \sqrt{t_n - t_{i-1}}} \tag{25}$$

Therefore the accuracy of computed heat flux is influenced by uncertainties in the temperature measurement and in the thermal properties of a material. It should be noted that only the temperature increment, $T'(t_i) = T(t_i) - T(t_0)$, is required to evaluate the heat flux from Eq. (25) and no magnitude of measured value is necessary. In this case, a series of bias errors are expected to be offset and only the random component is required to be accounted for. To properly estimate the precision limit of the heat flux data, in the present study, a Monte Carlo algorithm was newly developed. In this algorithm, the temperature data were randomly varied by a specified level of uncertainty and the overall uncertainty in the time-averaged heat flux was numerically estimated. By taking into account the data reduction process employed in the actual test, the random uncertainty component coming from the temperature measurement error was evaluated based on the following procedures.

1. Set a constant value of the surface heat flux q_0.
2. Obtain a baseline temperature time history $T_{0,i}$ by the following relation given from the exact solution of the one-dimensional heat conduction equation [6]

$$t_i = i\Delta t$$

$$T_{0,i} = \frac{2q_0}{\sqrt{\pi}}\sqrt{\frac{t_i}{\rho ck}}, \quad i = 0, \cdots, n$$

   where Δt is the time increment which corresponds to the data sampling frequency.
3. Set $l = 0$, where l is the number of iteration for the step 4 to 8.
4. Set the "noisy" temperature time history T_i as

$$T_i = T_{0,i} + \Delta T(2U - 1)$$

   where U is the random variable which takes a value between 0 and 1, and ΔT is the maximum level of random uncertainty.
5. Smooth the temperature time history by the moving average.
6. Obtain the heat flux time history from Eq. (25) for a set of "smoothed" T_i.
7. Compute time-averaged heat flux q^l_{av}.
8. Evaluate the variance as

$$\sigma^2 = \sum_{i=1}^{l}(q^i_{\mathrm{av}} - q_0)^2/l$$

9. Increment l as $l \rightarrow l + 1$ and repeat the step 4 to 8 until the level of the heat flux uncertainty (2σ for 95% coverage) converges to a constant value.

Care was taken such that each of the above uncertainty estimation process consistently follows the actual data reduction process. In the present study, the temperature random uncertainty ΔT was estimated from the experimental data as a standard deviation of the temperature scattering and was set to 0.2 degrees. The heat flux uncertainty corresponding to the specified ΔT was then computed by varying the level of surface heat flux from 1 to 100 kW/m^2. Note that the heat flux level of 1 and 100 kW/m^2 is the same order as the present experimental data obtained at the cylinder/flare and stagnation part of the model, respectively.

On the other hand, since the term concerning the thermal properties appears as a constant in Eq. (25), the thermal properties uncertainty was estimated as a bias limit. The coefficient $\sqrt{\rho ck}$ is rewritten as $\rho c\sqrt{\alpha}$, where α denotes thermal diffusivity. From the previous experience, the measurement uncertainty of ρ, c, and α were considered to be 1%, 1%, and 5%, respectively. Hence the uncertainty of $\sqrt{\rho ck}$ can be evaluated as 2.9%.

In summary, the overall heat flux uncertainty was estimated as a root-sum-square combination of the random component concerning the temperature measurement and the bias component concerning the thermal properties estimation. In Fig. 7, the estimated heat flux uncertainty as a function of the heat flux level is depicted.

It can be confirmed that, in the case of q_0 = 1 kW/m^2, the total uncertainty reaches up to 40%. As expected, the effect of temperature uncertainty becomes dominant as the level of heat flux decreases, while becomes negligible for the case of q_0 = 100 kW/m^2. The data smoothing reduces the heat flux uncertainty to a large extent for the low heating case. In fact, as much as 97% error was observed for the q_0 = 1 kW/m^2 case if the data were not smoothed. In this case, the temperature increase is of the order of 0.1 K, which is even smaller than the level of the temperature scattering specified. Hence, although the data are sufficiently smoothed by moving average, we cannot completely get rid of the random errors. On the contrary, for the high heating case, up to several ten degrees of temperature increase is noted. Hence the effect of temperature random uncertainty becomes negligible and we can obtain essentially identical results even though the data are not smoothed. Therefore the total heat flux estimation accuracy is essentially affected by only the level of uncertainty in the thermal properties.

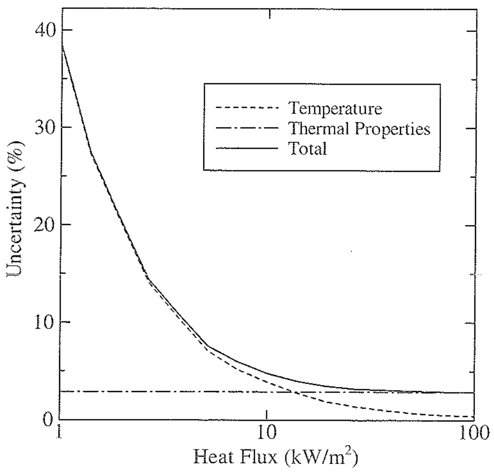

Fig. 7 Estimated heat flux errors versus the heat flux level.

6. RESULTS AND DISCUSSION

6.1 Force tests

The variation of the three-component aerodynamic coefficients C_{AF}, C_N, and C_m with respect to the angle of attack are shown in Figs. 8 to 15 for the nominal stagnation pressures of 1, 2.5, 4, and 6 MPa, respectively.

For the forebody axial force coefficient, the contribution of the base pressure correction term (see Eq. (1)) to the total value is shown to have, for example, a maximum of 4% for the case of P_0 = 6 MPa and hence cannot be neglected.

In Figs. 8, 10, 12, and 14, the predicted levels of uncertainty in

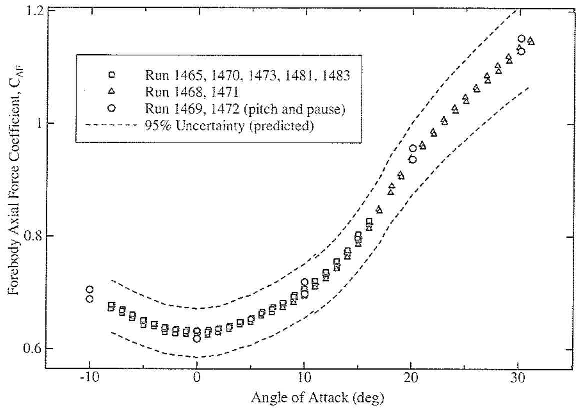

Fig. 8 Forebody axial force coefficient versus angle of attack (P_0 = 1 MPa).

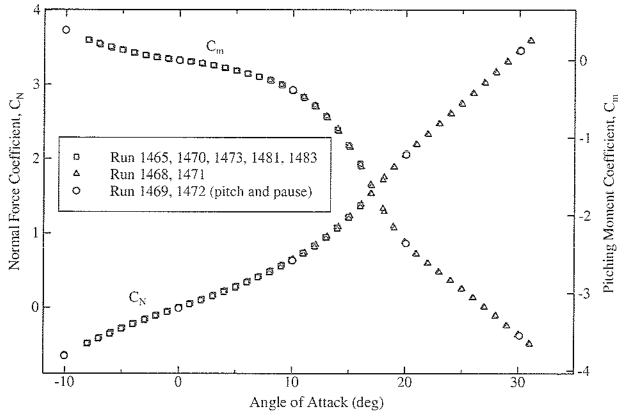

Fig. 9 Normal force and pitching moment coefficients versus angle of attack (P_0 = 1 MPa).

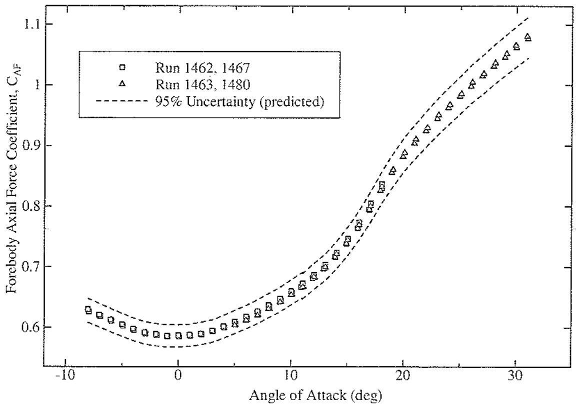

Fig. 10 Forebody axial force coefficient versus angle of attack (P_0 = 2.5 MPa).

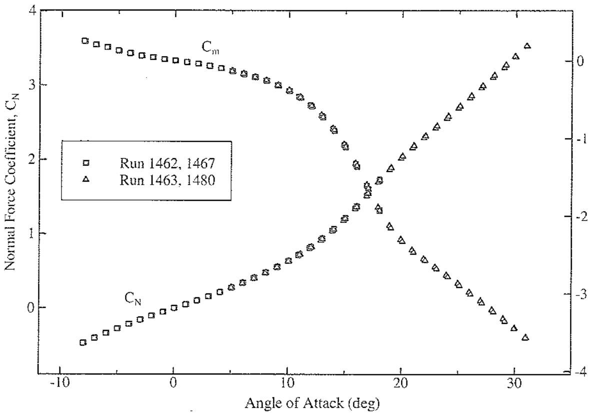

Fig. 11 Normal force and pitching moment coefficients versus angle of attack (P_0 = 2.5 MPa).

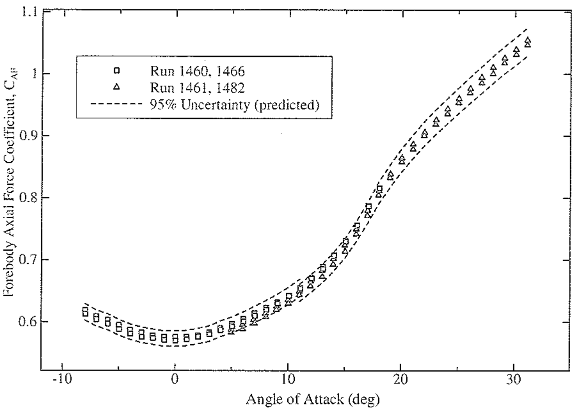

Fig. 12 Forebody axial force coefficient versus angle of attack (P_0 = 4 MPa).

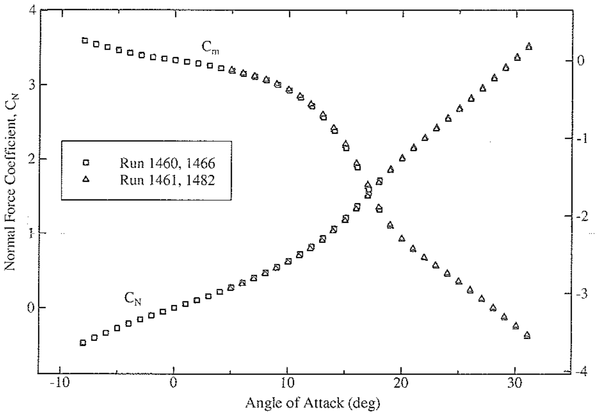

Fig. 13 Normal force and pitching moment coefficients versus angle of attack (P_0 = 4 MPa).

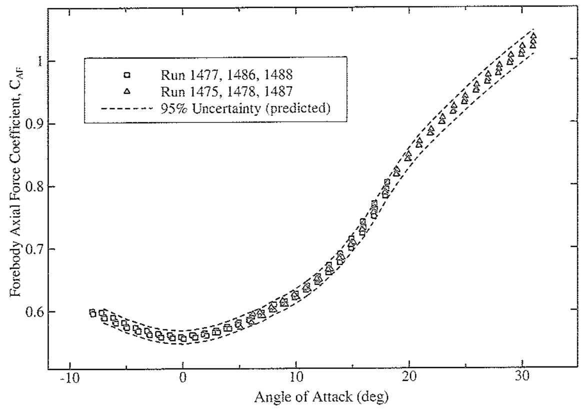

Fig. 14 Forebody axial force coefficient versus angle of attack ($P_0 = 6$ MPa).

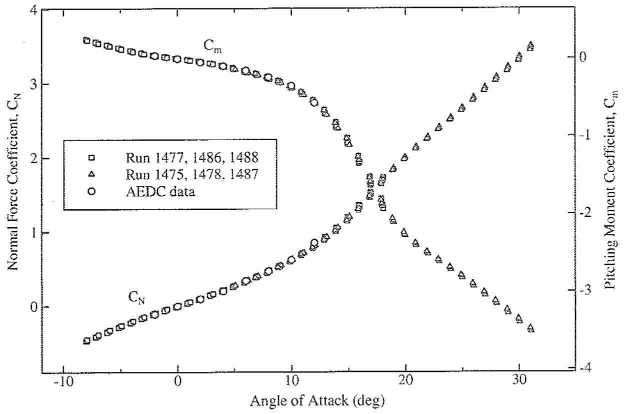

Fig. 15 Normal force and pitching moment coefficients versus angle of attack ($P_0 = 6$ MPa).

C_{AF} are also indicated. Although the level of uncertainty varies as the angle of attack changes, the minimum value at zero degrees was used for all angles of attack. The level of uncertainty for the case of P_0 = 1 MPa reaches up to 6% of the measurement value and decreases as the stagnation pressure increases. As far as the forebody axial force coefficient is concerned, the error element concerning the balance measurement is dominant for the overall uncertainty and hence the level of uncertainty increases as the aerodynamic force decreases, i.e., as the stagnation pressure decreases. For each level of the stagnation pressure, it can be confirmed that all data agreed well within the predicted uncertainty. Although a slight discrepancy is observed at the overlapped angles of attack between the low- and high-sweep operation mode, its discrepancy is much smaller than the level of uncertainty. As well, two pitch-and-pause data differs slightly as indicated in Fig. 8, but the difference is within the level of uncertainty range and is hence considered to be acceptable.

Table 5 Comparison of the predicted/experimentally-evaluated precision limits ($P_0 = 1$ MPa, $\alpha = 15$ deg).

	Estimated from uncertainty analysis	Obtained from 5 repeat runs
C_{AF}	0.021	0.011
C_N	0.030	0.018
C_m	0.028	0.024

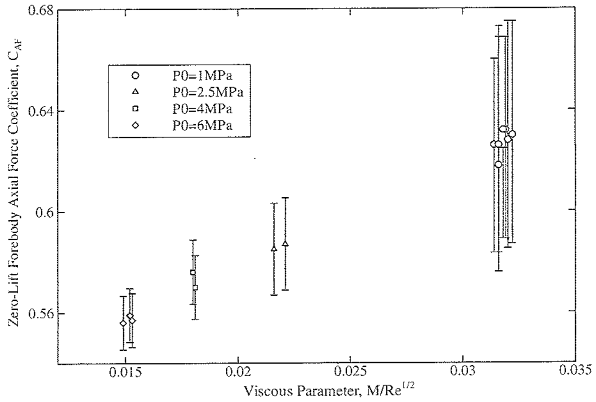

Fig. 16 Zero-lift axial-force coefficient versus viscous parameter.

Table 5 shows a comparison of the estimated/experimentally-evaluated precision limits of the three-component aerodynamic coefficients in the case of P_0 = 1 MPa and an angle of attack of 15 degrees. The experimental values were obtained from a total of five repeat runs with applying Eqs. (7) to (9).

Overall, the estimated precision limit is larger than the experimental value. This is presumably due to overestimation of the balance output errors.

For the case of P_0 = 6 MPa, the results are compared with data obtained at Arnold Engineering Development Center (AEDC) 50-inch Mach 10 Tunnel [2] as shown in Fig. 15. In this tunnel, the Reynolds number based on the centerbody diameter of the model is 1.36×10^6, which is much higher than the present HWT conditions (see Table C1). Excellent agreement is confirmed for the normal and pitching moment coefficients.

In Fig. 16, the zero-lift forebody axial force coefficient is plotted versus the viscous parameter defined as $M/\sqrt{Re}$. At hypersonic speeds, the wave drag (pressure integration) contribution to the total aerodynamic coefficient remains constant with Reynolds number variations, while the low local Reynolds number, which is caused by the increased bow-wave total pressure losses, produces a relatively large skin friction contribution [2]. Hence the axial force increases as the Reynolds number decreases.

Finally the three-component aerodynamic coefficients versus the angle of attack for each tunnel run are tabulated in detail in Table D1 of Appendix D.

6.2 Heat tests

In Fig. 17, the heat transfer coefficient distributions along the body surface obtained from the thermocouples are compared between the five repeat runs for the case of P_0 = 2.5 MPa at zero angle of attack. It is noted that the heat transfer coefficient data agree well in the nose part, while they are slightly scattered in the cylinder/flare junction part. In this region, the temperature increase is small due to relatively low heating and thus the S/N ratio of sensor output becomes degraded. This is, however, expected since up to 40% of uncertainty was evaluated at the heat flux level of 1 kW/m^2 in the preceding uncertainty analysis. On the other hand, the random errors in the nose part is less than 1% for every sensors and thus good repeatability is confirmed.

In Fig. 18, non-dimensional heat flux distributions (divided by the stagnation heat flux value) along the body surface are compared for the four levels of the stagnation pressure. As can be seen, the trend of the distribution is nearly identical for each P_0 and hence the effect of the reservoir pressure variation (i.e., Reynolds number) is found to be negligible in the present test condition range.

The axial distributions of the heat transfer coefficient for the model windward part at an angle of attack of 15 degrees are plotted for the case of P_0 = 2.5 MPa in Fig. 19 and for the comparison between each P_0 in Fig. 20, respectively. Compared to the zero angle of attack case, the level of aerodynamic heating is relatively high even in the cylinder/flare junction region and hence good repeatability is confirmed throughout the whole part.

Figure 21 indicates the comparison of heat flux distributions in the nose part between the data reduced from the co-axial thermocouples and those from the IR thermography. Good agreement is confirmed between the two measurement techniques, typically less than 3% discrepancy in the stagnation region. Since planar measurement is possible for the IR thermography technique, the data which have the same axial position were compared at zero angle of attack conditions. The result showed that the data scattering in the circumferential direction was typically less than 1% and hence was supposed to be negligible. As well, a set of data reduced from the different data acquisition time were compared

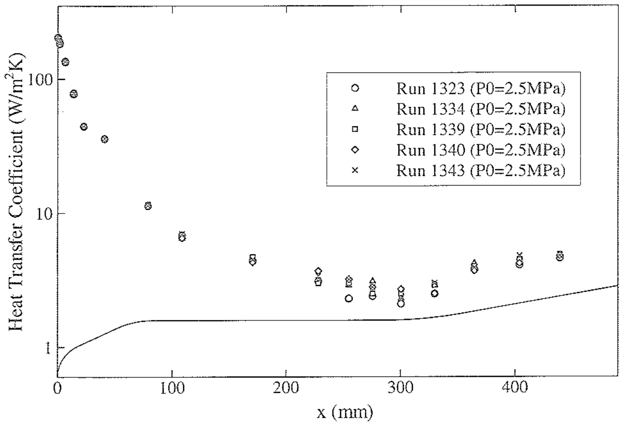

Fig. 17 Repeatability of the heat transfer coefficients (P_0= 2.5 MPa, α = 0 degrees).

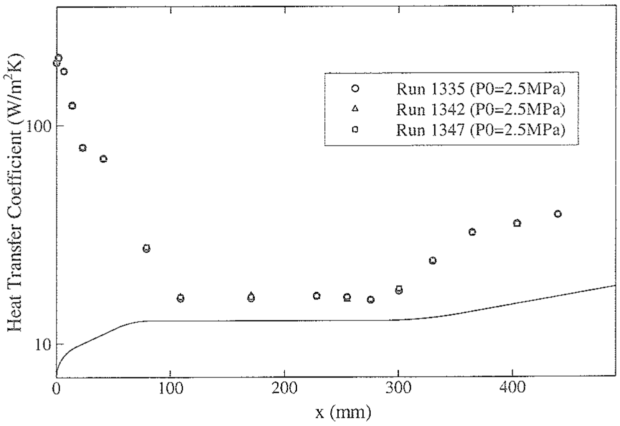

Fig. 19 Repeatability of the heat transfer coefficients (P_0= 2.5 MPa, α = 15 degrees).

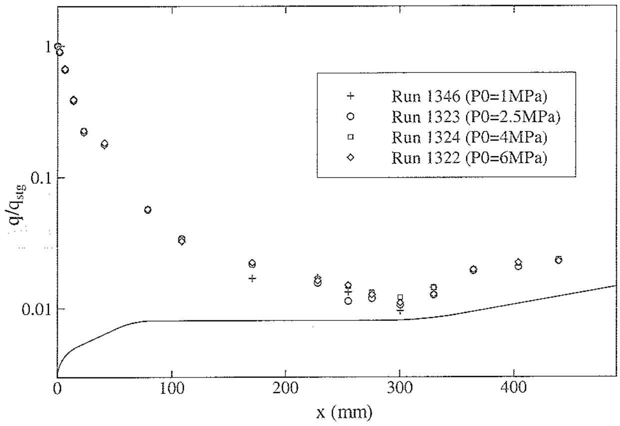

Fig. 18 Comparison of non-dimensional heat flux distributions for different stagnation pressures (α = 0 degrees).

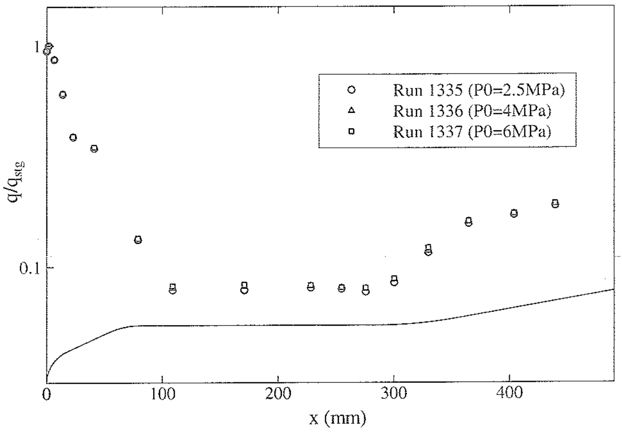

Fig. 20 Comparison of non-dimensional heat flux distributions for different stagnation pressures (α = 15 degrees).

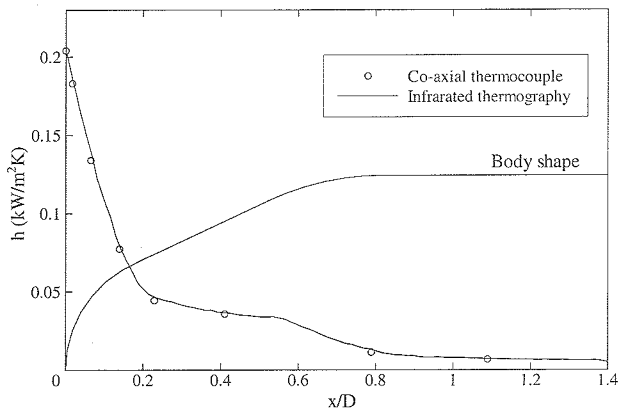

Fig. 21 Comparison of heat transfer rate distributions between thermocouple and IR thermography data (P_0 = 2.5 MPa, α = 0 degrees).

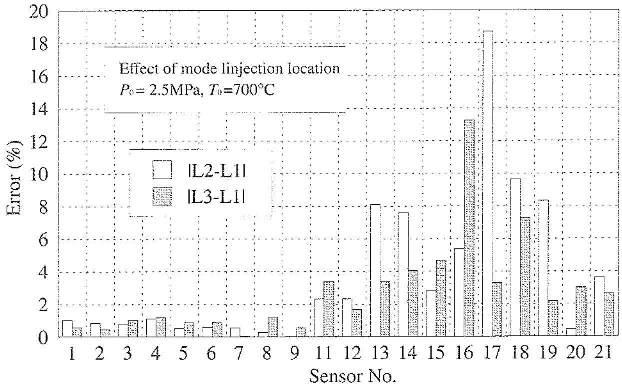

Fig. 23 Error distribution due to the change of model injection point (P_0 = 2.5 MPa).

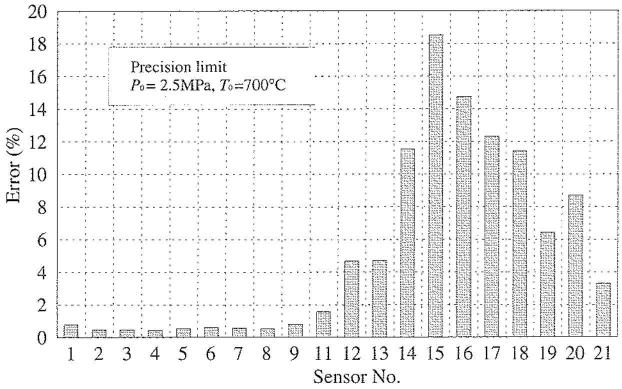

Fig. 22 Random error (precision limit) distribution obtained from the five repeat runs (P_0 = 2.5 MPa).

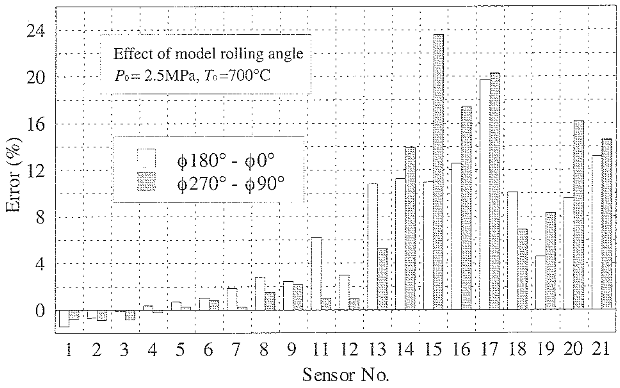

Fig. 24 Error distribution due to the change of model rotational angle (P_0 = 2.5 MPa).

and it appeared that the difference was also less than 1%. The reliability of the present data is thus enhanced by applying the two measurement techniques.

As already mentioned, a total of five repeat runs were made to evaluate uncertainties associated with flow repeatability. The precision limit for the heat transfer coefficient was derived by using Eqs. (7) to (9) and is illustrated for each sensor in Fig. 22 (data of sensor 10 are not included due to sensor trouble). As expected, a maximum uncertainty of up to 20% is noted around sensor 15, corresponding to the cylinder/flare junction point, due to low heating. For the case of P_0 = 2.5 MPa, the minimum heat flux level is around 1.5 kW/m^2. It should be noted from Fig. 7 that the predicted level of random uncertainty at this heat flux level is almost the same, indicating that the present Monte Carlo analysis estimates the heat flux uncertainty reasonably.

Next the effect of the test section flow non-uniformity on the measurement accuracy was examined by changing the model injection point and the result is shown in Fig. 23. The difference is less than 1% in the nose part and is the same order of the data repeatability as can be seen in Fig. 22. Therefore it appears that there is no significant effect concerning the change of the model injection location and, in other words, the flow field is sufficiently uniform in the stream-wise direction.

Next the data are compared at the zero angle of attack conditions by rotating the model around the body axis prior to the tunnel run. The rolling angle ϕ is defined as zero when the sensors in the cylindrical part (e.g. sensor 15) face upward. Then the model was rotated in the clockwise direction by 90, 180, and 270 degrees, viewed from the downstream. Two differences of the heat transfer coefficient between ϕ = 180 and 0 degrees and between ϕ = 270 and 90 degrees are shown for each sensor in Fig. 24.

As confirmed, the sign of the error changes from minus to plus at the sensor 4 (corresponds to the stagnation point). This implies that the model is slightly inclined relative to the free-stream such that sensors 1 to 3 (see Fig. A2 of Appendix A) faces upwind at ϕ = 0° and 90° even though the nominal angle of attack is zero. This is also confirmed from Fig. 25 which shows the distribution of the averaged heat transfer coefficient obtained from the five repeat runs for 8 sensors circumferentially placed in the flare

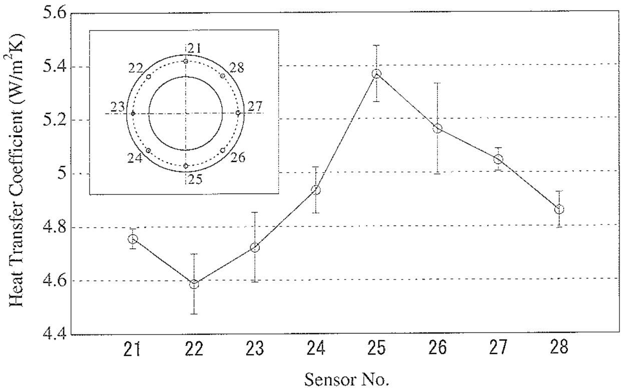

Fig. 25 Comparison of heat transfer coefficient in the azimuthal distribution at the flare part ($P_0 = 2.5$ MPa).

part.

The error bars shown in Fig. 25 denote the precision index concerning the averaged value. Considering the level of uncertainty, it is obvious that there is a systematic difference such that the heat transfer coefficient of the sensors 25 and 27 is much higher than that of the sensors 21 and 23, respectively. Hence it can be considered that the model is inclined relative to the free-stream so that sensors 25 and 27 face upwind. Considering the correspondence of the sensor locations between the nose and flare part (see Fig. A2), this is consistent with the result of Fig. 24. In fact, the actual model alignment angle at the zero angle of attack condition was measured in the present experiment using a level and 0.16 degrees of the model support error was confirmed. Since the degree of the scattering is found to be around 10%, we can conclude that the heat transfer coefficients in the flare part include 10% uncertainty produced by the model alignment error in addition to the random/bias errors contained in each sensor.

Finally, the present heat test data are summarized in detail for each sensor and tunnel run in Table D2.

6. CONCLUSIONS

As a series of the comparison test campaign between two hypersonic facilities in JAXA, force and heat flux measurements were conducted in the JAXA 1.27 m blow-down cold type hypersonic wind tunnel using the ballistic type standard model HB-2.

From the force test data obtained, good repeatability was confirmed for all of the tunnel conditions. The magnitude of measurement uncertainty was estimated using a statistical approach and it was observed that the scattering of the experimental data were reasonably included within the predicted uncertainty limits. The normal force and pitching moment data were also compared with existing experimental data conducted in the AEDC hypersonic wind tunnel, showing a good agreement.

As for the heat test, good repeatability in terms of the heat transfer coefficient was also confirmed concerning the heat transfer coefficient distribution along the model surface for the nose part, while a slight scattering was observed in the vicinity of the cylinder/flare junction part due to low heating. The precision limit was evaluated from the data of five repeat runs and it was found that the estimated value for the heat transfer coefficient is less than 1% for the high-heating and up to 20% in the low-heating part, respectively. The heat transfer coefficient obtained from the IR thermography agreed very well with the thermocouple data. From the data for eight sensors installed circumferentially in the flare part, it was shown that up to 10% of uncertainty in the heat transfer coefficient could exist due to model support error. Also performed was a Monte Carlo simulation to estimate the level of uncertainty in the time-averaged heat flux data reduction process. The result showed that the uncertainty in thermal properties is dominant for overall accuracy of the measurement data when the heating rate is sufficiently high (e.g. 100 kW/m^2). On the other hand, for a heat flux level of 1 kW/m^2, the effect of data scattering concerning the temperature measurement was found to become dominant. The predicted level of the precision limit in the low heating part showed a good agreement with that experimentally obtained from the five repeat runs.

Finally, since the data were carefully examined in terms of accuracy and were confirmed to be sufficiently reliable, the present force/heat test results are believed to provide useful information as a database for the validation of hypersonic CFD codes.

ACKNOWLEDGMENTS

The authors would like to thank Mr. Shigeo Kayaba and Mr. Muneyoshi Nakagawa for their contributions to the present test campaign. One of the authors would also like to thank Dr. Keisuke Fujii for the valuable discussion concerning the heat flux reduction process using the co-axial themocouple.

REFERENCES

1) Nomura, S., Sakakibara, S., Hozumi K., and Soga, K., "NAL New Hypersonic Wind Tunnel System," AIAA Paper AIAA 93-5006, Dec. 1993.
2) Gray, J. D., "Summary Report on Aerodynamic Characteristics of Standard Models HB-1 and HB-2," AEDC-TDR-64-137, July 1964. 25.
3) Kidd, C.T., Nelson C.G., and Scott, W.T., "Extraneous Thermoelectric EMF Effects Resulting from the Press-Fit Installation of Coaxial Thermocouples in Metal Models," *Pro-*

ceedings of the 40th International Instrumentation Symposium, Baltimore, MD, May 1994, pp. 317–335.

4) Aeschliman, D.P. and Oberkampf, W.L., "Experimental Methodology for Computational Fluid Dynamics Code Validation," *AIAA J.*, Vol. 36, No. 6, May 1998, pp. 733-741.
5) Cook, W. J., and Felderman, E. J., "Reduction of Data from Thin-Film Heat-Transfer Gages: A Concise Numerical Technique," *AIAA J.*, Vol. 4, No. 3, March 1966, pp. 561–562.
6) Schultz, D.L., and Jones, T. V., "Heat Transfer Measurements in Short Duration Hypersonic Facilities," AGARDograph 165, 1973.
7) Sundqvist, B., "Thermal Diffusivity and Thermal Conductivity of Chromel, Alumel, and Constantan in the range 100.450K," *J. Appl. Phys.*, Vol. 72, No. 2, July 1992, pp. 539.
8) Jones, R. A., and Hunt, J. L., "Use of Fusible Temperature Indicator for Obtaining Quantitative Aerodynamic Heat-Transfer Data," NASA TR R-230, 1966.
9) Merski, N. R., "Global Aeroheating Wind-Tunnel Measurements Using Improved Two-Color Phosphor Thermography Method," *AIAA J.,* Vol. 36, No. 2, March-April 1999, pp. 160–170.
10) *Assessment of Wind Tunnel Data Uncertainty*, AIAA Standard S-071-1995, AIAA, Washington, DC, 1995.
11) *Measurement Uncertainty,* ASME Performance Test Codes, Supplement on Instruments and Apparatus, Part 1, ANSI/ASME PTC19.1-1985, 1985.
12) Boudreau, A. H., "Performance and Operational Characteristics of AEDC/VKF Tunnels A, B, and C," AEDC-TR-80-48, 1981.
13) Ames research staff, "Equations, Tables, and Charts for Compressible Flow," NACA Report 1135, 1954

Appendix A
Detail of the force/heat model

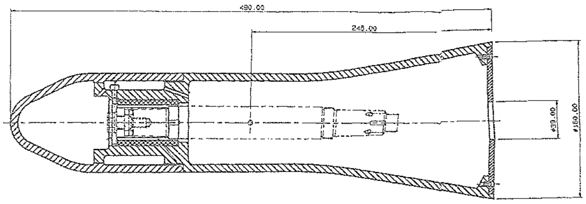

Fig. A1 Detailed drawing of HB-2 force model.

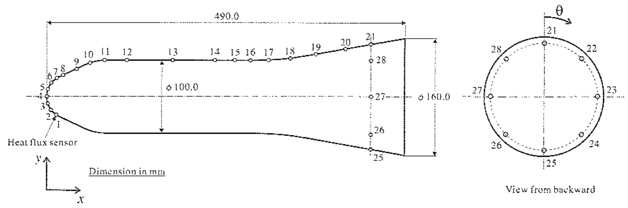

Fig. A2 Sensor location of HB-2 heat model.

Table A1 Heat flux sensor location.

Sensor No.	x (mm)	y (mm)	θ (deg)
1	13.9	-25.3	0.0
2	6.5	-18.6	0.0
3	1.7	-9.9	0.0
4	0.0	0.0	0.0
5	1.7	9.9	0.0
6	6.5	18.6	0.0
7	13.9	25.3	0.0
8	22.9	29.8	0.0
9	41.0	38.2	0.0
10	59.3	46.3	0.0
11	78.9	49.9	0.0
12	108.9	50.0	0.0
13	170.7	50.0	0.0
14	228.1	50.0	0.0
15	254.8	50.0	0.0
16	275.6	50.0	0.0
17	300.4	50.3	0.0
18	329.8	52.5	0.0
19	364.6	57.9	0.0
20	404.0	64.9	0.0
21	439.3	71.1	0.0
22	439.3	50.3	45
23	439.3	0.0	90
24	439.3	-50.3	135
25	439.3	-71.1	180
26	439.3	-50.3	225
27	439.3	0.0	270
28	439.3	50.3	315

Appendix B
Computation of free-stream properties in HWT

In reducing the free-stream properties for a conventional cold type hypersonic wind tunnel, one approach accepted widely is to assume an isentropic expansion from the reservoir to the test section. In this case, the free-stream conditions can be computed from the stagnation pressure P_0, stagnation temperature T_0, and pitot pressure P_{pit}.

The following one-dimensional isentropic formulas provide relations between the stagnation and free-stream flow properties as functions of the Mach number [13]

$$\left(\frac{P_{pit}}{P_0}\right)_{perfect}=\left[\frac{(\gamma+1)M^2}{(\gamma-1)M^2+2}\right]^{\frac{\gamma}{\gamma-1}}\left[\frac{\gamma}{2\gamma M^2-(\gamma-1)}\right]^{\frac{\gamma}{\gamma-1}} \tag{B1}$$

$$\left(\frac{P_\infty}{P_0}\right)_{perfect}=\left[1+\frac{\gamma-1}{2}M^2\right]^{\frac{\gamma}{\gamma-1}} \tag{B2}$$

$$\left(\frac{T_\infty}{T_0}\right)_{perfect}=\left[1+\frac{\gamma-1}{2}M^2\right]^{-1} \tag{B3}$$

where $\gamma = 1.4$ is the specific heat ratio and the subscript "perfect" denotes perfect gas (i.e., "ideal" property). Note that these relations hold only for perfect gas flows. In a hypersonic wind tunnel, the stagnation pressure and temperature are high so that effects of intermolecular force and vibrational energy excitation become not negligible. To take into account such real gas effects, the following formulas found in Ref. [12] give useful correlation factors applicable for a range of calorically and thermally imperfect gases:

$$\left(\frac{P_\infty}{P_0}\right)_{real}\Big/\left(\frac{P_\infty}{P_0}\right)_{perfect}=1.0562+49.57\times10^{-6}P_0$$
$$-(3523+1.8300P_0+1.3839T_0-0.0002196P_0T_0)\times10^{-8}T_0 \tag{B4}$$

$$\left(\frac{T_\infty}{T_0}\right)_{real}\Big/\left(\frac{T_\infty}{T_0}\right)_{perfect}=0.9378-3.900\times10^{-6}P_0$$
$$+(6533+0.6547P_0-0.4137T_0-0.0001354P_0T_0)\times10^{-8}T_0 \tag{B5}$$

$$\left(\frac{P_{pit}}{P_0}\right)_{real}\Big/\left(\frac{P_{pit}}{P_0}\right)_{perfect}=1.0419+38.31\times10^{-6}P_0$$
$$-(1968+0.7925P_0+1.6905T_0)\times10^{-8}T_0 \tag{B6}$$

where the subscript "real" denotes real gas (i.e., "measured" property) and the unit of P_0 and T_0 are psi and °R, respectively (1 psi = 1/6894.76 Pa and 1 °R = 9/5 K). By converting the "real" (measured) properties to the "perfect" (ideal) values, it becomes possible to apply the perfect gas isentropic relations Eqs. (B1) to (B3). The above correlation factors were calculated based on the Beattie-Bridgeman equation of state with considering the vibrational relaxation.

The local Mach number M_i found in Eq. (15) is computed by the following procedure:

1. Evaluate $(P_{pit}/P_0)_{real}$ from the measured P_0 and P_{pit}.
2. Obtain $(P_{pit}/P_0)_{perfect}$ from Eq. (B6).
3. Compute M_i from Eq. (B1). Since Eq. (B1) is a nonlinear equation with respect to M, it should be solved using an iterative technique.

Thus the free-stream Mach number M_∞ is calculated as an average of the local Mach number obtained at each point in the test section as shown in Eq. (15).

On the other hand, the free-stream conditions for the present force/heat test were computed from P_0 and T_0 measured at each tunnel run plus the Mach number obtained as above. The detailed procedures are listed below.

1. Obtain $(p_\infty/P_0)_{perfect}$ and $(T_\infty/T_0)_{perfect}$ from the specified M_∞ and Eqs. (B2) and (B3).
2. Obtain $(p_\infty/P_0)_{real}$ and $(T_\infty/T_0)_{real}$ from Eqs. (B4) and (B5).
3. Obtain p_∞ and T_∞ as $p_\infty = (p_\infty/P_0)_{real} \times P_0$ and $T_\infty = (T_\infty/T_0)_{real} \times T_0$.
4. Compute the dynamic pressure q_∞ from the following relation.

$$q_\infty=\frac{\gamma}{2}p_\infty M_\infty^2 \tag{B7}$$

The free-stream conditions tabulated in Tables C1 and C2 of Appendix C were computed by following the present procedure.

Appendix C

Tables of the operating and free-stream conditions

Table C1 Summery of tunnel/free-stream conditions for the force test.

Run No.	P_0 (MPa)	T_0 (K)	M_∞	ρ_∞ (g/m^3)	p_∞ (Pa)	T_∞ (K)	U_∞ (m/s)	Re (× 10^5)	α (deg)	Remarks
1460	4.036	1040.3	9.65	7.22	115.1	55.5	1441.6	2.86	- 10 → 18	
1461	4.036	1040.1	9.65	7.23	115.2	55.5	1441.4	2.86	4 → 32	
1462	2.515	994.6	9.59	4.88	75.0	53.5	1405.8	1.97	- 10 → 18	
1463	2.515	999.9	9.59	4.85	74.9	53.8	1409.8	1.95	4 → 32	
1465	1.000	957.6	9.46	2.16	32.7	52.6	1375.6	0.87	- 10 → 16	
1466	4.028	1044.4	9.65	7.17	114.8	55.8	1444.7	2.84	- 10 → 18	
1467	2.514	1020.2	9.59	4.73	74.6	55.0	1425.4	1.88	- 10 → 18	
1468	1.000	957.8	9.46	2.16	32.6	52.6	1375.8	0.87	6 → 32	
1469	1.001	953.9	9.46	2.17	32.7	52.4	1372.7	0.88	-10, 0, 10, 20, 30	Pitch & Pause
1470	1.001	938.8	9.46	2.22	32.8	51.5	1360.9	0.91	- 10 → 16	
1471	0.999	934.9	9.46	2.22	32.7	51.3	1357.8	0.91	6 → 32	
1472	0.999	942.7	9.46	2.20	32.7	51.7	1364.0	0.90	-10, 0, 10, 20, 30	Pitch & Pause
1473	1.000	944.5	9.46	2.20	32.7	51.8	1365.4	0.90	- 10 → 16	
1475	6.056	1068.5	9.69	10.3	168.4	56.8	1463.8	4.05	4 → 32	
1477	6.058	1044.5	9.69	10.6	169.2	55.4	1445.8	4.24	- 10 → 18	
1478	6.055	1041.9	9.69	10.7	169.2	55.3	1443.8	4.26	4 → 32	
1480	2.512	1002.6	9.59	4.83	74.8	53.9	1411.9	1.94	4 → 32	
1481	0.997	960.9	9.46	2.15	32.5	52.8	1378.2	0.86	- 10 → 16	
1482	4.028	1022.9	9.65	7.37	115.3	54.5	1428.4	2.96	4 → 32	
1483	0.997	947.3	9.46	2.18	32.6	52.0	1367.6	0.89	- 10 → 16	
1486	6.052	1073.3	9.69	10.3	168.1	57.1	1467.4	4.01	- 10 → 18	
1487	6.050	1075.3	9.69	10.2	168.0	57.2	1468.9	4.00	34 → 6	Negative sweep
1488	6.051	1069.4	9.69	10.3	168.2	56.8	1464.5	4.04	20 → - 8	Negative sweep

Reynolds number is based on the centerbody diameter of the model (100mm)

Table C2 Summery of tunnel/free-stream conditions for the heat test.

Run No.	P_0 (MPa)	T_0 (K)	M_∞	ρ_∞ (g/m^3)	p_∞ (Pa)	T_∞ (K)	U_∞ (m/s)	Re (×10^5)	α (deg)	ϕ (deg)	L	Remarks
1322	6.044	1068.8	9.69	10.3	168.1	56.8	1464.1	4.04	0	0	L1	
1323	2.514	1021.5	9.59	4.72	74.6	55.1	1426.3	1.87	0	0	L1	
1324	4.022	1014.9	9.65	7.43	115.2	54.1	1422.3	3.00	0	0	L1	
1329	2.517	1032.5	9.59	4.66	74.6	55.7	1434.7	1.83	0	0	L2	
1330	2.515	1027.4	9.59	4.69	74.6	55.4	1430.8	1.85	0	0	L3	
1331	2.513	998.6	9.59	4.85	74.8	53.7	1408.9	1.96	0	180	L1	
1332	2.509	1008.1	9.59	4.79	74.6	54.3	1416.1	1.92	0	90	L1	
1333	2.509	1002.2	9.59	4.83	74.7	53.9	1411.6	1.94	0	270	L1	
1334	2.509	984.3	9.59	4.94	74.9	52.9	1397.8	2.01	0	0	L1	
1335	2.513	995.9	9.59	4.87	74.9	53.6	1406.8	1.97	15	0	L1	
1336	4.021	1040.7	9.65	7.19	114.7	55.6	1441.9	2.85	15	0	L1	
1337	6.040	1049.8	9.69	10.5	168.5	55.7	1449.8	4.19	15	0	L1	
1338	2.511	999.9	9.59	4.85	74.8	53.8	1409.8	1.95	15	180	L1	
1339	2.512	1025.8	9.59	4.69	74.5	55.3	1429.6	1.85	0	0	L1	
1340	2.509	996.0	9.59	4.86	74.8	53.6	1406.9	1.96	0	0	L1	
1341	2.508	1002.8	9.59	4.82	74.7	54.0	1412.1	1.94	0	180	L1	
1342	2.514	1008.1	9.59	4.80	74.8	54.3	1416.1	1.92	15	0	L1	
1343	2.512	986.4	9.59	4.93	75.0	53.0	1399.4	2.00	0	0	L1	
1346	0.998	919.9	9.46	2.27	32.8	50.4	1346.0	0.94	0	0	L1	
1347	2.514	1015.3	9.59	4.76	74.7	54.7	1421.6	1.89	15	0	L1	
1348	0.997	941.2	9.46	2.20	32.6	51.7	1362.8	0.90	0	0	L1	
1349	2.508	981.1	9.59	4.95	74.9	52.7	1395.4	2.02	0	0	L1	IR Camera
1350	0.996	934.6	9.46	2.22	32.6	51.3	1357.6	0.91	0	0	L1	IR Camera
1351	4.020	1049.9	9.65	7.11	114.5	56.1	1448.8	2.80	0	0	L1	IR Camera
1352	6.044	1008.3	9.69	11.1	169.9	53.3	1418.3	4.54	0	0	L1	IR Camera
1353	2.510	1007.6	9.59	4.80	74.7	54.2	1415.7	1.92	0	0	L1	IR Camera
1354	2.512	999.6	9.59	4.85	74.8	53.8	1409.6	1.95	15	0	L1	IR Camera

Reynolds number is based on the centerbody diameter of the model (100mm)
L1: 500 mm from the nozzle exit, L2: 270 mm, L3: 950 mm

Appendix D

Tables of the force/heat experimental data

Table D1 Summary of force test results.

Run 1460			
α (deg)	C_{AF}	C_N	C_m
-8.00	0.619	-0.474	0.253
-7.01	0.609	-0.405	0.207
-6.00	0.603	-0.341	0.170
-4.99	0.595	-0.276	0.133
-4.00	0.587	-0.215	0.097
-2.99	0.583	-0.159	0.066
-1.99	0.578	-0.104	0.039
-0.98	0.576	-0.051	0.018
0.01	0.576	-0.001	0.000
1.01	0.576	0.052	-0.021
2.01	0.578	0.103	-0.042
3.02	0.583	0.158	-0.069
4.02	0.590	0.217	-0.102
5.03	0.597	0.278	-0.137
6.03	0.605	0.341	-0.173
7.03	0.614	0.407	-0.212
8.04	0.623	0.477	-0.259
9.04	0.632	0.553	-0.313
10.04	0.642	0.633	-0.385
11.05	0.655	0.725	-0.476
12.05	0.671	0.826	-0.589
13.05	0.689	0.941	-0.732
14.05	0.708	1.069	-0.909
15.06	0.731	1.213	-1.122
16.06	0.756	1.372	-1.371
17.07	0.788	1.553	-1.662

Run 1461			
α (deg)	C_{AF}	C_N	C_m
4.97	0.588	0.272	-0.132
5.97	0.596	0.333	-0.168
6.96	0.604	0.398	-0.206
7.97	0.614	0.468	-0.252
8.98	0.626	0.544	-0.308
9.98	0.636	0.624	-0.377
10.98	0.650	0.715	-0.465
11.99	0.666	0.815	-0.577
12.99	0.683	0.928	-0.717
13.99	0.702	1.055	-0.888
14.99	0.724	1.195	-1.096
16.00	0.750	1.355	-1.346
17.00	0.780	1.528	-1.622
18.00	0.812	1.709	-1.910
19.01	0.839	1.873	-2.131
20.01	0.865	2.025	-2.301
21.01	0.887	2.165	-2.435
22.02	0.906	2.298	-2.542
23.02	0.926	2.431	-2.647
24.03	0.944	2.562	-2.750
25.04	0.961	2.694	-2.854
26.04	0.977	2.831	-2.965
27.04	0.995	2.968	-3.077
28.05	1.011	3.109	-3.195
29.06	1.026	3.248	-3.311
30.07	1.040	3.385	-3.428
31.07	1.055	3.529	-3.550

Run 1462			
α (deg)	C_{AF}	C_N	C_m
-7.92	0.626	-0.467	0.246
-6.93	0.619	-0.399	0.203
-5.93	0.611	-0.336	0.170
-4.93	0.603	-0.272	0.127
-3.92	0.596	-0.212	0.095
-2.91	0.590	-0.155	0.063
-1.91	0.587	-0.101	0.041
-0.92	0.585	-0.049	0.015
0.06	0.585	0.001	-0.002
1.07	0.586	0.052	-0.021
2.07	0.589	0.105	-0.041
3.08	0.594	0.161	-0.070
4.08	0.600	0.218	-0.100
5.08	0.607	0.279	-0.138
6.09	0.615	0.343	-0.175
7.08	0.625	0.409	-0.214
8.09	0.634	0.480	-0.261
9.10	0.645	0.557	-0.321
10.10	0.657	0.639	-0.391
10.90	0.667	0.711	-0.462
11.90	0.682	0.811	-0.574
12.91	0.698	0.922	-0.709
13.91	0.717	1.047	-0.878
14.91	0.739	1.188	-1.083
15.92	0.764	1.344	-1.327
16.92	0.795	1.520	-1.609
18.06	0.831	1.720	-1.920

Run 1463			
α (deg)	C_{AF}	C_N	C_m
5.09	0.604	0.280	-0.137
6.08	0.613	0.343	-0.173
7.08	0.621	0.409	-0.213
8.09	0.631	0.478	-0.258
9.10	0.643	0.555	-0.318
10.09	0.655	0.636	-0.387
11.10	0.668	0.729	-0.480
12.10	0.683	0.828	-0.590
12.90	0.697	0.916	-0.701
13.90	0.717	1.042	-0.868
14.90	0.739	1.184	-1.075
15.91	0.765	1.342	-1.320
16.91	0.795	1.517	-1.597
17.91	0.826	1.697	-1.886
18.92	0.856	1.866	-2.124
19.92	0.882	2.020	-2.300
20.92	0.904	2.160	-2.436
21.93	0.925	2.295	-2.552
22.94	0.945	2.429	-2.656
23.94	0.963	2.560	-2.760
24.94	0.982	2.696	-2.867
25.95	0.998	2.832	-2.977
26.95	1.015	2.968	-3.089
27.95	1.031	3.107	-3.206
28.96	1.046	3.243	-3.319
29.97	1.062	3.387	-3.441
30.97	1.077	3.528	-3.560

Run 1465			
α (deg)	C_{AF}	C_N	C_m
-8.07	0.675	-0.481	0.257
-7.07	0.666	-0.414	0.213
-6.06	0.654	-0.345	0.166
-5.06	0.650	-0.277	0.131
-4.06	0.642	-0.215	0.093
-3.05	0.635	-0.155	0.063
-2.05	0.633	-0.102	0.038
-1.05	0.631	-0.051	0.022
-0.05	0.628	0.001	0.000
0.94	0.631	0.052	-0.015
1.94	0.631	0.105	-0.041
2.95	0.638	0.161	-0.065
3.95	0.643	0.220	-0.101
4.96	0.652	0.281	-0.132
5.96	0.660	0.346	-0.168
6.95	0.670	0.413	-0.209
7.96	0.682	0.485	-0.260
8.96	0.693	0.561	-0.315
9.97	0.707	0.646	-0.390
10.97	0.721	0.738	-0.477
11.97	0.737	0.839	-0.584
12.97	0.754	0.952	-0.727
13.97	0.772	1.076	-0.900
14.98	0.796	1.221	-1.107
15.97	0.825	1.379	-1.353

Run 1466			
α (deg)	C_{AF}	C_N	C_m
-7.98	0.613	-0.468	0.248
-6.98	0.604	-0.401	0.203
-5.98	0.597	-0.335	0.166
-4.98	0.588	-0.272	0.127
-3.97	0.581	-0.212	0.094
-2.96	0.576	-0.156	0.063
-1.96	0.574	-0.102	0.039
-0.96	0.571	-0.051	0.017
0.03	0.570	-0.001	-0.001
1.04	0.572	0.051	-0.020
2.03	0.576	0.102	-0.041
3.04	0.580	0.157	-0.070
4.04	0.587	0.216	-0.101
5.05	0.593	0.276	-0.137
6.06	0.601	0.338	-0.173
7.05	0.610	0.405	-0.212
8.06	0.620	0.475	-0.258
9.07	0.630	0.551	-0.317
10.07	0.642	0.633	-0.387
11.08	0.654	0.724	-0.479
12.08	0.670	0.825	-0.590
13.08	0.686	0.939	-0.734
14.07	0.707	1.067	-0.908
15.08	0.730	1.215	-1.129
16.09	0.756	1.372	-1.377
17.09	0.787	1.549	-1.660
18.04	0.816	1.717	-1.919

Run 1467			
α (deg)	C_{AF}	C_N	C_m
-8.02	0.630	-0.470	0.251
-7.02	0.621	-0.403	0.205
-6.01	0.613	-0.338	0.168
-5.01	0.605	-0.275	0.129
-4.01	0.598	-0.215	0.094
-3.00	0.592	-0.158	0.062
-2.00	0.589	-0.104	0.040
-0.99	0.586	-0.052	0.018
0.00	0.587	-0.001	-0.001
1.00	0.588	0.050	-0.020
2.00	0.590	0.102	-0.040
3.01	0.595	0.158	-0.067
4.01	0.602	0.215	-0.100
5.02	0.610	0.276	-0.135
6.02	0.618	0.339	-0.172
7.01	0.627	0.406	-0.212
8.02	0.637	0.477	-0.258
9.03	0.648	0.553	-0.318
10.03	0.660	0.636	-0.387
11.04	0.673	0.727	-0.478
12.03	0.687	0.826	-0.587
13.04	0.704	0.940	-0.729
14.04	0.724	1.068	-0.905
15.05	0.747	1.213	-1.118
16.05	0.774	1.374	-1.367
17.06	0.805	1.552	-1.653
18.05	0.837	1.730	-1.933

Run 1468			
α (deg)	C_{AF}	C_N	C_m
8.07	0.680	0.488	-0.266
9.07	0.691	0.566	-0.326
10.08	0.704	0.652	-0.396
11.08	0.717	0.741	-0.487
12.08	0.734	0.848	-0.603
13.08	0.752	0.961	-0.747
14.08	0.774	1.088	-0.916
15.09	0.800	1.234	-1.124
16.09	0.825	1.392	-1.376
16.90	0.849	1.536	-1.599
18.10	0.890	1.758	-1.952
18.91	0.911	1.891	-2.141
19.91	0.940	2.053	-2.338
20.90	0.964	2.200	-2.492
21.92	0.987	2.340	-2.617
22.92	1.008	2.475	-2.723
23.92	1.029	2.616	-2.841
24.92	1.048	2.754	-2.949
25.93	1.065	2.891	-3.062
26.93	1.086	3.034	-3.177
27.93	1.104	3.178	-3.300
28.94	1.120	3.319	-3.417
29.94	1.136	3.460	-3.535
30.95	1.150	3.600	-3.647

Run 1469			
α (deg)	C_{AF}	C_N	C_m
-10.04	0.705	-0.643	0.383
-0.01	0.632	-0.003	-0.004
10.00	0.719	0.640	-0.385
20.05	0.957	2.067	-2.361
30.12	1.153	3.467	-3.546

Run 1470			
α (deg)	C_{AF}	C_N	C_m
-8.03	0.673	-0.492	0.260
-5.02	0.642	-0.290	0.127
-4.03	0.639	-0.228	0.099
-3.02	0.629	-0.171	0.061
-2.02	0.629	-0.118	0.046
-1.02	0.626	-0.065	0.018
-0.02	0.626	-0.015	0.008
0.97	0.625	0.038	-0.017
1.97	0.629	0.092	-0.036
2.98	0.635	0.148	-0.065
3.98	0.644	0.208	-0.094
4.98	0.648	0.267	-0.132
5.99	0.659	0.332	-0.168
6.98	0.667	0.401	-0.212
7.99	0.680	0.473	-0.255
8.99	0.689	0.552	-0.323
10.00	0.702	0.634	-0.386
11.00	0.716	0.725	-0.481
12.01	0.730	0.823	-0.585
13.01	0.745	0.937	-0.734
14.01	0.769	1.065	-0.901
15.01	0.794	1.212	-1.114
16.01	0.821	1.365	-1.342

Run 1471			
α (deg)	C_{AF}	C_N	C_m
7.97	0.673	0.465	-0.256
10.98	0.710	0.716	-0.474
11.98	0.724	0.817	-0.583
12.98	0.742	0.930	-0.720
13.98	0.763	1.054	-0.885
14.98	0.786	1.199	-1.105
15.99	0.814	1.356	-1.339
16.99	0.845	1.533	-1.620
18.00	0.878	1.718	-1.910
19.00	0.906	1.891	-2.165
20.00	0.935	2.048	-2.345
21.00	0.959	2.194	-2.498
22.01	0.982	2.332	-2.615
23.01	1.003	2.471	-2.733
24.02	1.023	2.606	-2.838
25.02	1.040	2.740	-2.945
26.02	1.061	2.881	-3.059
27.02	1.077	3.023	-3.181
28.03	1.094	3.162	-3.287
29.03	1.112	3.308	-3.422
30.04	1.129	3.447	-3.528
31.05	1.145	3.594	-3.656

Run 1472			
α (deg)	C_{AF}	C_N	C_m
-10.04	0.688	-0.652	0.384
20.05	0.937	2.059	-2.361
30.12	1.130	3.460	-3.547

Table D1 Summary of force test results. (continued)

Run 1473			
α (deg)	C_{AF}	C_N	C_m
-8.08	0.671	-0.492	0.263
-7.07	0.664	-0.422	0.216
-6.06	0.655	-0.356	0.173
-5.06	0.649	-0.290	0.135
-4.06	0.641	-0.226	0.091
-3.06	0.635	-0.171	0.065
-2.05	0.627	-0.117	0.041
-1.05	0.627	-0.064	0.023
-0.05	0.626	-0.011	0.000
0.95	0.627	0.041	-0.017
1.94	0.630	0.094	-0.037
2.95	0.636	0.150	-0.061
3.95	0.644	0.209	-0.093
4.96	0.650	0.271	-0.137
5.96	0.659	0.335	-0.171
6.96	0.665	0.401	-0.208
7.97	0.674	0.472	-0.258
8.97	0.687	0.549	-0.311
9.97	0.698	0.631	-0.389
10.98	0.714	0.725	-0.476
11.98	0.732	0.828	-0.594
12.98	0.748	0.939	-0.726
13.98	0.769	1.064	-0.891
14.99	0.794	1.212	-1.105
15.97	0.822	1.363	-1.333

Run 1475			
α (deg)	C_{AF}	C_N	C_m
4.89	0.580	0.266	-0.124
5.91	0.586	0.328	-0.165
6.91	0.594	0.392	-0.203
7.92	0.603	0.460	-0.246
8.92	0.612	0.534	-0.301
9.93	0.623	0.613	-0.368
10.93	0.637	0.702	-0.455
11.93	0.651	0.800	-0.562
12.93	0.668	0.912	-0.700
13.93	0.686	1.037	-0.870
14.94	0.709	1.179	-1.080
15.94	0.734	1.335	-1.324
16.95	0.764	1.507	-1.601
17.95	0.796	1.690	-1.889
18.96	0.824	1.854	-2.110
19.96	0.849	2.003	-2.277
20.95	0.870	2.142	-2.409
21.97	0.889	2.273	-2.515
22.98	0.908	2.404	-2.616
23.99	0.926	2.534	-2.717
24.99	0.942	2.667	-2.822
25.99	0.960	2.804	-2.933
27.00	0.976	2.941	-3.046
28.01	0.991	3.080	-3.160
29.02	1.007	3.218	-3.278
30.03	1.021	3.357	-3.395
31.03	1.036	3.501	-3.517

Run 1477			
α (deg)	C_{AF}	C_N	C_m
-7.93	0.596	-0.453	0.238
-6.94	0.589	-0.386	0.197
-5.93	0.581	-0.323	0.161
-4.93	0.574	-0.262	0.126
-3.93	0.568	-0.203	0.092
-2.92	0.562	-0.147	0.061
-1.91	0.558	-0.094	0.036
-0.91	0.557	-0.043	0.016
0.08	0.556	0.006	-0.002
1.09	0.558	0.056	-0.022
2.09	0.561	0.107	-0.043
3.10	0.566	0.162	-0.070
4.10	0.572	0.219	-0.102
4.91	0.578	0.267	-0.129
5.91	0.585	0.329	-0.166
6.91	0.593	0.393	-0.203
7.92	0.602	0.462	-0.248
8.92	0.612	0.537	-0.302
9.93	0.623	0.617	-0.371
10.94	0.636	0.706	-0.458
11.94	0.649	0.804	-0.568
12.94	0.666	0.915	-0.703
13.96	0.685	1.042	-0.878
14.96	0.707	1.182	-1.084
15.98	0.733	1.340	-1.333
16.98	0.762	1.513	-1.609
17.99	0.794	1.693	-1.893

Run 1478			
α (deg)	C_{AF}	C_N	C_m
5.08	0.574	0.278	-0.135
6.07	0.582	0.338	-0.171
7.07	0.592	0.403	-0.209
8.08	0.601	0.472	-0.254
9.09	0.610	0.547	-0.310
10.08	0.622	0.627	-0.380
11.09	0.634	0.715	-0.468
12.09	0.650	0.816	-0.582
13.09	0.666	0.929	-0.723
14.09	0.685	1.056	-0.898
15.10	0.709	1.200	-1.112
15.91	0.729	1.326	-1.310
16.91	0.759	1.499	-1.586
17.91	0.790	1.677	-1.870
18.92	0.818	1.841	-2.092
19.93	0.842	1.989	-2.261
20.92	0.863	2.127	-2.390
21.94	0.883	2.259	-2.500
22.94	0.901	2.388	-2.598
23.95	0.919	2.518	-2.699
24.96	0.936	2.650	-2.805
25.96	0.953	2.786	-2.914
26.97	0.969	2.921	-3.024
27.97	0.985	3.061	-3.142
28.98	0.999	3.197	-3.256
29.99	1.013	3.333	-3.370
31.00	1.028	3.475	-3.491

Run 1480			
α (deg)	C_{AF}	C_N	C_m
5.01	0.604	0.277	-0.132
6.01	0.612	0.337	-0.168
7.01	0.620	0.401	-0.211
8.01	0.631	0.472	-0.253
9.02	0.642	0.551	-0.316
10.02	0.654	0.631	-0.380
11.03	0.667	0.721	-0.472
12.03	0.684	0.822	-0.581
13.03	0.700	0.936	-0.724
14.03	0.722	1.062	-0.891
15.03	0.745	1.208	-1.110
16.04	0.770	1.366	-1.355
17.04	0.801	1.545	-1.642
18.05	0.833	1.725	-1.925
19.05	0.861	1.893	-2.153
20.06	0.889	2.047	-2.325
21.05	0.911	2.188	-2.465
22.07	0.930	2.319	-2.571
23.07	0.951	2.453	-2.678
24.07	0.968	2.586	-2.781
25.08	0.986	2.721	-2.892
26.08	1.005	2.863	-3.004
27.08	1.019	2.996	-3.118
28.09	1.037	3.138	-3.233
29.10	1.052	3.277	-3.353
29.91	1.066	3.392	-3.449
30.91	1.081	3.533	-3.567

Run 1481			
α (deg)	C_{AF}	C_N	C_m
-7.93	0.678	-0.475	0.255
-6.94	0.670	-0.399	0.200
-5.93	0.659	-0.332	0.158
-4.93	0.651	-0.270	0.128
-3.93	0.644	-0.210	0.089
-2.92	0.638	-0.151	0.060
-1.92	0.635	-0.099	0.032
-0.92	0.634	-0.044	0.012
0.07	0.630	0.006	-0.007
1.08	0.634	0.059	-0.018
2.07	0.636	0.114	-0.047
3.08	0.641	0.169	-0.069
4.08	0.648	0.228	-0.104
5.09	0.655	0.291	-0.139
6.09	0.666	0.356	-0.176
7.09	0.674	0.424	-0.217
8.09	0.682	0.495	-0.266
9.10	0.696	0.574	-0.327
9.90	0.703	0.640	-0.389
10.90	0.721	0.732	-0.475
11.90	0.734	0.832	-0.591
12.91	0.755	0.945	-0.718
13.91	0.772	1.077	-0.898
14.91	0.798	1.216	-1.095
15.95	0.827	1.377	-1.340

Run 1482			
α (deg)	C_{AF}	C_N	C_m
4.96	0.583	0.262	-0.123
6.00	0.589	0.325	-0.164
7.01	0.598	0.391	-0.203
8.01	0.608	0.459	-0.247
8.95	0.620	0.534	-0.302
10.00	0.630	0.615	-0.372
10.97	0.644	0.702	-0.456
11.96	0.658	0.800	-0.562
13.00	0.673	0.910	-0.696
13.96	0.693	1.035	-0.866
15.01	0.714	1.176	-1.073
15.99	0.742	1.334	-1.320
16.98	0.772	1.508	-1.597
17.96	0.805	1.691	-1.887
18.97	0.833	1.855	-2.111
20.00	0.858	2.009	-2.289
20.99	0.879	2.146	-2.417
21.97	0.901	2.281	-2.532
22.97	0.919	2.411	-2.631
24.02	0.936	2.541	-2.735
25.00	0.954	2.674	-2.837
26.01	0.970	2.810	-2.949
27.04	0.986	2.947	-3.062
28.05	1.001	3.084	-3.178
29.04	1.018	3.225	-3.294
30.08	1.032	3.363	-3.411
31.06	1.047	3.503	-3.529

Run 1483			
α (deg)	C_{AF}	C_N	C_m
-8.05	0.678	-0.481	0.260
-7.05	0.668	-0.415	0.213
-6.04	0.661	-0.352	0.174
-5.04	0.651	-0.285	0.128
-4.04	0.644	-0.225	0.099
-3.03	0.638	-0.165	0.064
-2.03	0.634	-0.108	0.036
-1.03	0.631	-0.056	0.017
-0.03	0.632	-0.006	-0.001
0.96	0.630	0.048	-0.022
1.96	0.635	0.101	-0.037
2.97	0.639	0.155	-0.064
3.97	0.648	0.215	-0.097
4.98	0.653	0.277	-0.138
5.98	0.663	0.343	-0.176
6.98	0.671	0.410	-0.216
7.98	0.682	0.482	-0.260
8.99	0.693	0.560	-0.324
9.99	0.707	0.643	-0.391
10.99	0.721	0.738	-0.488
12.00	0.736	0.838	-0.596
13.00	0.756	0.951	-0.737
14.00	0.776	1.081	-0.908
15.00	0.804	1.227	-1.117
16.01	0.828	1.381	-1.345

Run 1486			
α (deg)	C_{AF}	C_N	C_m
-8.01	0.600	-0.466	0.251
-7.01	0.591	-0.399	0.205
-6.03	0.584	-0.334	0.167
-5.02	0.576	-0.272	0.131
-4.02	0.570	-0.212	0.096
-3.01	0.564	-0.156	0.065
-2.08	0.562	-0.102	0.041
-1.05	0.559	-0.051	0.020
0.01	0.557	-0.001	0.000
0.94	0.561	0.049	-0.019
1.93	0.565	0.100	-0.038
2.96	0.569	0.155	-0.065
3.92	0.575	0.212	-0.097
4.94	0.582	0.271	-0.132
6.12	0.591	0.346	-0.174
6.96	0.597	0.397	-0.205
8.07	0.610	0.481	-0.259
9.03	0.615	0.542	-0.306
9.98	0.627	0.623	-0.375
10.98	0.640	0.713	-0.463
11.94	0.655	0.811	-0.572
12.93	0.673	0.924	-0.712
13.91	0.691	1.049	-0.883
14.92	0.715	1.194	-1.096
15.91	0.742	1.354	-1.345
16.94	0.771	1.528	-1.627
18.05	0.805	1.726	-1.934

Run 1487			
α (deg)	C_{AF}	C_N	C_m
6.22	0.595	0.351	-0.175
6.81	0.598	0.385	-0.194
7.81	0.606	0.452	-0.237
8.82	0.616	0.526	-0.288
9.83	0.626	0.604	-0.353
10.83	0.637	0.690	-0.434
11.83	0.651	0.786	-0.537
12.84	0.666	0.893	-0.666
13.83	0.684	1.015	-0.829
14.85	0.705	1.152	-1.027
15.84	0.729	1.304	-1.264
16.85	0.757	1.473	-1.533
17.85	0.788	1.653	-1.822
18.85	0.817	1.822	-2.061
19.86	0.841	1.974	-2.241
20.87	0.863	2.113	-2.378
21.87	0.882	2.245	-2.492
22.88	0.900	2.374	-2.590
23.89	0.917	2.502	-2.691
24.89	0.932	2.629	-2.791
25.91	0.950	2.767	-2.901
26.91	0.964	2.898	-3.010
27.90	0.978	3.033	-3.122
28.92	0.994	3.166	-3.235
29.93	1.007	3.303	-3.353
30.98	1.020	3.443	-3.478

Run 1488			
α (deg)	C_{AF}	C_N	C_m
-7.20	0.598	-0.416	0.217
-6.19	0.590	-0.350	0.177
-5.19	0.582	-0.287	0.141
-4.18	0.574	-0.226	0.107
-3.18	0.569	-0.169	0.075
-2.18	0.564	-0.114	0.046
-1.17	0.562	-0.063	0.026
-0.17	0.559	-0.012	0.005
0.82	0.562	0.038	-0.012
1.83	0.563	0.089	-0.033
2.83	0.566	0.142	-0.058
3.84	0.572	0.198	-0.088
4.84	0.579	0.256	-0.120
5.85	0.586	0.318	-0.157
6.85	0.593	0.382	-0.194
7.86	0.602	0.449	-0.235
8.86	0.611	0.523	-0.288
9.87	0.621	0.599	-0.352
10.87	0.633	0.686	-0.433
11.88	0.646	0.781	-0.535
12.88	0.661	0.887	-0.664
13.88	0.677	1.005	-0.822
14.89	0.700	1.145	-1.024
15.88	0.724	1.295	-1.259
16.89	0.751	1.462	-1.527
17.89	0.783	1.647	-1.808

Table D2 Summary of heat test results.

Sensor No.	Heat Flux (kW/m^2)													
	1322	1323	1324	1327	1328	1331	1332	1333	1334	1335	1336	1337	1338	1339
1	91.72	56.21	70.03	55.90	55.76	53.95	55.22	54.13	53.51	29.59	39.15	48.36	84.36	55.94
2	157.22	96.36	118.84	94.91	95.40	92.97	94.72	92.75	91.52	61.89	81.57	100.63	120.62	95.93
3	214.26	132.71	163.88	131.03	131.47	129.20	131.11	128.41	126.77	104.13	136.24	167.52	140.90	132.61
4	232.08	143.96	177.88	142.51	143.32	140.88	142.32	140.16	137.62	132.33	173.15	212.44	132.58	144.23
5	209.36	129.41	160.26	128.20	128.59	127.05	127.87	126.54	123.76	139.36	182.23	222.81	100.89	129.44
6	155.01	95.22	118.18	94.47	94.78	93.79	94.14	93.66	90.99	121.33	158.80	194.40	61.68	95.17
7	90.50	55.44	69.09	55.15	55.41	55.14	55.19	54.62	52.93	85.22	112.22	137.91	29.77	55.68
8	52.55	31.90	40.35	31.91	32.10	32.14	31.74	31.82	30.59	54.93	72.03	89.15	15.17	32.30
9	42.46	25.73	32.21	25.56	25.72	25.86	25.50	25.73	24.92	48.92	64.44	79.78	11.03	25.93
11	13.27	8.16	10.22	8.22	8.22	8.50	8.30	8.26	7.83	19.00	25.09	31.11	2.59	8.42
12	7.55	4.91	6.00	4.56	5.08	4.82	4.82	4.83	4.48	11.26	15.13	19.00	1.14	4.81
13	5.18	3.14	3.79	3.11	3.08	3.47	3.13	3.30	3.02	11.23	15.41	19.23	1.02	3.42
14	3.77	2.24	3.00	2.15	2.57	2.55	2.20	2.47	2.16	11.52	15.47	19.19	2.42	2.14
15	3.48	1.62	2.63	2.16	2.16	2.29	1.95	2.39	2.01	11.41	15.16	18.73	3.01	2.17
16	2.95	1.69	2.33	1.95	2.14	2.17	1.88	2.19	2.14	11.04	15.05	18.68	3.31	1.83
17	2.53	1.54	2.14	1.94	1.98	2.01	1.74	2.06	1.58	12.19	16.54	20.51	4.42	1.80
18	2.95	1.88	2.57	2.12	2.04	2.12	1.85	1.93	1.97	16.61	22.21	28.19	5.81	2.08
19	4.57	2.78	3.52	2.71	2.78	2.90	2.63	2.83	2.88	22.48	30.24	37.22	7.72	2.94
20	5.18	2.95	3.88	3.06	2.78	3.41	3.23	3.70	3.19	24.63	32.71	40.25	7.78	3.27
21	5.28	3.31	4.18	3.11	3.25	3.81	3.21	3.62	3.32	27.01	36.12	44.57	7.21	3.54
22	5.50	3.15	4.18	3.31	3.38	3.83	3.35	3.45	3.22	16.97	22.72	28.01	0.92	3.30
23	5.26	3.26	4.10	3.23	3.46	3.79	3.66	3.30	3.17	5.99	7.41	9.06	5.97	3.34
24	5.71	3.57	4.39	3.56	3.64	3.38	3.74	3.15	3.35	0.93	1.01	1.20	17.26	3.68
25	6.25	3.86	5.03	3.55	3.85	3.26	3.66	3.44	3.95	6.84	9.72	12.09	26.89	3.92
26	6.39	3.76	5.03	3.91	3.80	3.37	3.81	3.37	3.36	0.92	1.00	1.04	17.01	3.92
27	5.86	3.54	4.72	3.51	3.78	3.50	3.21	3.56	3.37	6.13	7.69	9.03	5.97	3.64
28	5.68	3.40	4.42	3.40	3.77	3.40	3.23	3.74	3.26	17.08	22.56	27.87	0.70	3.35

Sensor No.	Heat Flux (kW/m^2)												
	1340	1341	1342	1343	1346	1347	1348	1349	1350	1351	1352	1353	1354
1	54.62	54.03	29.57	53.95	31.95	30.22	32.79	*	*	*	*	*	*
2	92.95	92.87	61.83	91.89	54.92	62.95	56.09	*	*	*	*	*	*
3	128.67	128.84	104.03	127.08	76.09	106.33	77.97	*	*	*	*	*	*
4	139.80	140.60	132.62	137.92	83.05	135.23	84.91	*	*	*	*	*	*
5	125.60	126.76	139.44	124.17	74.58	142.08	76.08	*	*	*	*	*	*
6	92.70	93.67	121.85	91.30	54.60	123.93	55.77	*	*	*	*	*	*
7	54.13	54.99	85.52	53.22	31.57	87.01	32.32	*	*	*	*	*	*
8	31.07	32.31	54.84	30.78	18.09	56.34	18.75	*	*	*	*	*	*
9	25.20	25.90	49.13	24.82	14.50	49.99	15.00	*	*	*	*	*	*
11	7.88	8.50	19.16	7.86	4.76	19.82	4.97	*	*	*	*	*	*
12	4.53	4.87	11.56	4.84	2.65	11.67	2.67	*	*	*	*	*	*
13	3.04	3.77	11.72	3.06	1.40	11.65	1.85	3.14	1.93	4.34	5.13	3.26	11.91
14	2.55	2.64	11.55	2.33	1.42	11.83	1.55	2.30	1.40	3.05	3.65	2.61	11.69
15	2.23	2.28	11.23	2.25	1.11	11.65	1.47	2.01	1.45	2.68	3.26	2.05	11.50
16	1.97	2.11	11.13	1.92	1.04	11.40	1.35	2.05	1.28	2.65	3.13	1.98	11.37
17	1.86	2.02	12.29	1.59	0.77	12.76	1.21	2.04	1.07	2.54	2.75	1.84	12.67
18	1.75	2.16	16.89	2.05	1.19	17.11	1.41	2.03	1.22	2.49	2.77	1.98	17.07
19	2.62	3.03	22.65	2.67	1.63	22.90	1.74	2.81	1.87	3.75	4.30	2.65	22.88
20	2.91	3.24	24.55	3.30	1.74	25.03	1.58	3.32	1.88	4.40	4.69	3.15	24.80
21	3.33	3.93	27.15	3.35	1.88	27.66	1.85	3.46	1.75	4.44	5.25	3.16	27.14
22	3.09	3.47	17.29	3.22	1.79	17.49	1.87	3.23	2.11	4.23	5.20	3.21	17.14
23	3.48	3.46	6.02	3.38	2.08	5.85	2.08	3.33	2.16	4.74	4.98	3.31	5.83
24	3.33	3.53	1.00	3.41	1.82	1.16	2.05	3.39	2.52	4.51	5.76	3.62	0.87
25	3.60	3.42	6.92	3.70	2.19	7.10	2.10	3.66	2.51	5.27	5.99	3.87	7.22
26	3.63	3.59	0.69	3.53	2.21	1.19	1.83	3.75	2.26	4.78	5.65	3.47	0.92
27	3.46	3.51	5.85	3.42	2.12	6.02	2.19	3.59	2.07	5.02	5.41	3.79	6.05
28	3.42	3.38	17.19	3.29	1.69	17.43	2.04	3.45	2.11	4.54	5.08	3.11	17.36

JAXA Research and Development Report
(JAXA-RR-04-035E)

Date of Issue: March 31, 2005

Edited and Published by:
Japan Aerospace Explortion Agency
7-44-1 Jindaiji-higashimachi, Chofu-shi,
Tokyo 182-8522 Japan

Printed by:
TOKYO PRESS Co., Ltd.
2-27-12 Sakuragawa, Itabashi-ku, Tokyo 174-0075 Japan

Japan Aerospace Exploration Agency